

Changes in southern ocean ventilation inferred from repeat hydrographies: a maximum entropy approach

Author:

Ting, Yu-Heng

Publication Date:

2015

DOI:

<https://doi.org/10.26190/unsworks/2802>

License:

<https://creativecommons.org/licenses/by-nc-nd/3.0/au/>

Link to license to see what you are allowed to do with this resource.

Downloaded from <http://hdl.handle.net/1959.4/54814> in <https://unsworks.unsw.edu.au> on 2025-08-06



CHANGES IN SOUTHERN OCEAN VENTILATION INFERRED FROM REPEAT HYDROGRAPHIES: A MAXIMUM ENTROPY APPROACH

Yu-Heng Ting

Supervisor: Associate Professor Mark Holzer

School of Mathematics and Statistics
The University of New South Wales

August 2015

SUBMITTED IN FULFILMENT OF THE REQUIREMENTS OF THE DEGREE OF
MASTER OF SCIENCE

Abstract

This thesis investigates the ventilation of the Southern Ocean in terms of its state in the early 1990s, its decadal changes from the 1990s to the early 2000s, and the implications of these changes for anthropogenic carbon (C_{ANT}) storage. A maximum entropy (ME) approach is used to deconvolve tracer measurements to estimate the boundary propagator, which is the joint distribution of the locations and times since last ventilation. We use Southern Ocean data from five meridional repeat hydrography sections (P16, P18, A16, I8S/I9N and S3) of the World Ocean Circulation Experiment and the Climate Variability and Predictability project for CFC-11, CFC-12, temperature, salinity, oxygen, and phosphate, as well as data from the Global Ocean Data Analysis Project (GLODAP) for radiocarbon, combined with surface histories derived from atmospheric CFC-11 and CFC-12 measurements and the World Ocean Atlas and GLODAP databases. We quantify Southern Ocean ventilation in terms of the water-mass fraction older than 30 years, the fractions of water last ventilated in specific regions that tile the global ocean surface, the global and regional mean transit times, and the width-to-mean ratio Δ/Γ of the global transit-time distribution (TTD). By independently deconvolving the original and repeat hydroographies for the boundary propagator, we find that Circumpolar Deep Water (CDW) has become older with a narrower TTD and an increased fraction last ventilated in the North Atlantic. Subantarctic Mode Water (SAMW) has become younger with a broader TTD and an increased fraction last ventilated in the Southern Ocean. Antarctic Bottom Water (AABW) has become younger. The inferred decadal changes

in ventilation are consistent with increased upwelling of CDW and enhanced SAMW formation driven by strengthened mid-latitude westerly winds. The inferred boundary propagators are used to propagate C_{ANT} into the ocean interior assuming constant disequilibrium. We estimate that the section-averaged water-column C_{ANT} storage per unit area has increased by $0.56 \pm 0.02 \text{ mol m}^{-2} \text{ yr}^{-1}$ in the 60°S – 20°S latitude strip along the sections. The changes in C_{ANT} storage due to changes in ventilation correspond to a pronounced increase of C_{ANT} in SAMW. There are no significant changes in C_{ANT} for CDW due to changes in ventilation. The net effect of the changes in ventilation contributes $0.08 \pm 0.02 \text{ mol m}^{-2} \text{ yr}^{-1}$ to the C_{ANT} storage rate in the Southern Ocean.

Dedication

I would like to dedicate this to my father Chien-Yuan, who always has high regard for my mathematical ability, and my mother Pi-Shuang, who fuels me with good food during thesis writing. Their support through the three years of the completion of this thesis has been much needed and appreciated. And also thanks to my God, who has refocused me time and time again.

Acknowledgment

I would like to thank my supervisor Mark Holzer, who has provided me extensive help with his experience in the field as well as in thesis writing. Mark helps me to constantly help me back to the greater picture when I need directions.

I acknowledge support from the Coastal Carbon Cluster CSIRO Flagship Collaboration for a scholarship, conference travel, and a visit to CSIRO/CMAR in Hobart. I also acknowledge conference travel support from my supervisor's ARC grant DP120100674.

Contents

Chapter 1	Introduction	1
1.1	Motivation	1
1.2	Background	4
1.2.1	Southern Ocean water masses and ventilation dynamics .	4
1.2.2	Anthropogenic carbon in the ocean	6
Chapter 2	Methods	9
2.1	Previous work	9
2.2	The boundary propagator \mathcal{G}	10
2.3	The principle of Maximum Entropy (ME)	12
Chapter 3	Data	20
3.1	Surface history data	20
3.2	Interior Data	21
3.3	C_{ANT} data	22
3.4	Choice of Prior	23
3.5	Uncertainty estimation	24
Chapter 4	Results	25
4.1	The Boundary Propagator \mathcal{G}	25
4.1.1	Base state in early 1990s	26
4.1.2	Decadal changes between early 1990s and mid-2000s . .	35
4.2	Application: C_{ANT} storage rate in the Southern Ocean . . .	45

Chapter 5	Discussions and Conclusions	56
Appendix A	Details of MEM set up	66
A.1	Discretization details	66
A.2	Standardizing C^S and C^I	66
A.3	Fsolve set up	68
A.4	Perturbation of the prior	69
Appendix B	Determination of an optimal ‘nominal year’ for GLODAP transient tracers	71
Appendix C	Supplementary figures	74
Bibliography		76

CHAPTER 1

Introduction

1.1 Motivation

Ventilation is the exchange of surface waters with the ocean interior.

This thesis is concerned with surface-to-interior ventilation, a fundamental aspect of the ocean circulation important for the role of the ocean in the global climate system and for controlling biogeochemical cycles. In the surface mixed layer, water interacts with the atmosphere through heat, freshwater and soluble gas exchanges. As water is subducted beneath the mixed-layer into the ocean interior in response to a combination of buoyancy and wind forcings, it transports momentum, thermal energy, nutrients and dissolved gases to depth. Ventilation, through its control on nutrient supply, has important implications on the ocean's ecosystem and biological productivity [e.g., *Sarmiento et al.*, 2004; *Holzer and Primeau*, 2013]. Moreover, ocean ventilation also plays an important role in the earth's global energy budget, as thermal energy and CO₂ are taken from the atmosphere and sequestered in the deep ocean with a wide spectrum of residence times [e.g., *Talley*, 2003; *Sabine et al.*, 2004].

Recent studies show that the Southern Hemisphere wind system is changing on decadal timescales. The Southern Annular Mode (SAM), a dominant mode of atmospheric variability in the Southern Hemisphere [*Gong and Wang*, 1999] is exhibiting a trend toward its positive phase in austral summer ¹, characterized by strengthening and poleward-intensifying mid-latitude westerlies

¹And perhaps also in austral autumn and spring, though the trends are less clear.

[e.g., *Marshall*, 2003; *Fogt et al.*, 2009; *Swart and Fyfe*, 2012]. The Southern-Hemisphere wind system has been identified to play an important role in ventilating the Southern Ocean, is thought to control the magnitude of the North Atlantic Deep Water (NADW) formation [*Toggweiler and Samuels*, 1993], and in turn believed to be an important modifier of the global overturning circulation [*Toggweiler and Samuels*, 1995]. It is therefore paramount to capture and quantify any corresponding changes in the ocean transport.

Many studies use models to identify possible oceanic responses to a poleward-strengthened mid-latitude westerlies. Increased upwelling of Circumpolar Deep Water (CDW) [*Russell et al.*, 2006; *Lovenduski et al.*, 2007], greater northward Ekman drift into the Subantarctic Mode Water (SAMW), decrease in SAMW ideal mean age and increased Antarctic Intermediate Water (AAIW) formation rate [*Oke and England*, 2004; *Waugh*, 2014] are expected. The increased wind stress also has implications on the oceanic eddy field and the strength of the Antarctic Circumpolar Current [ACC; *Meredith and Hogg*, 2006; *Hogg et al.*, 2014]. In terms of the carbon budget, the enhanced ventilation would in turn expose more deep water, which is rich in dissolved inorganic carbon (DIC) but deficient in anthropogenic carbon (C_{ANT}), to the atmosphere, and would increase (decrease) storage of DIC (C_{ANT}) in the deep waters [*Russell et al.*, 2006; *Lovenduski et al.*, 2007]. These decadal changes in the wind stress are thought to be crucial at a time where anthropogenic warming is expected. The strengthening wind maintains the current meridional overturning circulation (MOC), whereas anthropogenic warming increases stratification and inhibits overturning [*Toggweiler and Russell*, 2008]. Increased wind stress also could act to counter the reduced C_{ANT} uptake of the Southern Ocean due to anthropogenic warming [*Sarmiento et al.*, 1998].

Observational studies have also been performed to look for these changes in the Southern Ocean. *Tanhua et al.* [2013] exploited the similarity of early

1990s CFC-12 and late 2000s sulfur-hexafluoride (SF_6) atmospheric time history to identify changes in the ventilation characteristics of southeast Pacific SAMW. *Waugh et al.* [2013] and *Waugh* [2014] applied a transit-time-distribution (TTD) method to CFC-12 tracer measurements and employed a data-assimilated ocean model to infer an increase (decrease) in the ideal mean age of polar CDW (subtropical SAMW) for multiple sections in the Southern Ocean. However, both *Tanhua et al.* [2013] and *Waugh* [2014]'s TTD method are restricted to temporal changes. In their methodology, a single dominant surface tracer source is assumed and hence no spatial change information is obtainable. The methodology of *Waugh et al.* [2013] and *Waugh* [2014] are also restrictive in that they assumed the TTD of an interior water parcel [or the age spectrum; *Hall and Plumb*, 1994] to be inverse-Gaussian² distributed with only one free parameter.

This thesis sets out to use a maximum-entropy (ME) method to quantify (1) the initial base state of the surface-to-interior ocean transport in early 1990s and (2) changes in the surface-to-interior ocean transport between early 1990s to mid-2000s by decoding the information contained in repeat hydroographies, and (3) total decadal changes in C_{ANT} in the Southern Ocean, as well as decadal changes are exclusively due to changes in ventilation. We extend the previous observational studies by incorporating additional observed tracers and by accounting for the dependence of ventilation on surface location by finer surface discretization than previously done. Also, the need to assume a fixed functional form on the TTD is avoided. For C_{ANT} , the use of repeat hydrography data enables us to separate the transport-related C_{ANT} change from changes attributable to the rising atmospheric C_{ANT} , which is to the best of our knowledge not done previously.

²An inverse-Gaussian (IG) distribution is the distribution of the transit time of a particle in an advective and diffusive flow, and is defined by two parameters: its mean (Γ) and width (Δ).

The remainder of this thesis is organized as follows: Section 1.2 briefly reviews our current knowledge on Southern Ocean water masses, their dynamics and their importance in the global climate (Section 1.2.1), as well as the challenges faced in quantifying C_{ANT} in the ocean (Section 1.2.2). Chapter 2 gives an introduction on the use of tracers to obtain ventilation information, leading to the boundary-propagator framework and our maximum-entropy implementation, as well as explaining in detail the innovations and improvements of such approach over the existing studies. Chapter 3 outlines the observational data used. Results on the changes in the ventilation are documented in Chapter 4, with discussions and conclusion in Chapter 5.

1.2 Background

1.2.1 *Southern Ocean water masses and ventilation dynamics*

The Southern Ocean extends from the shores of Antarctica to a nominal northern boundary that varies among definitions but generally lies between 40°S and 30°S. It is unique among the world oceans in that it features a latitude band which has no longitudinal boundary (i.e., the meridional extent of the Drake Passage), where water extends zonally around the globe. This has several implications. First, the lack of obstructing landmasses gives rises to the very strong Southern Hemisphere mid-latitude westerly winds. Secondly, the strong mid-latitude westerly winds indirectly drives the eastward-flowing Antarctic Circumpolar Current (ACC, a.k.a West Wind Drift) within the Southern Ocean [Trenberth *et al.*, 1990]. With exceptions of some microcontinents like the Kerguelen Plateau, the ACC flows unobstructed and is the world's largest ocean current. Thirdly, the prevalent westerly winds also induce northward Ekman drift in all longitudes. The lack of land boundaries means that the geostrophic southward return flow across the Southern Ocean can only exist at depth, where bottom topography can support the zonal pressure gradient [Rintoul *et al.*, 2001].

The Southern Ocean is regarded as an important component in the global meridional overturning circulations, in that it is one of the main regions in the world where deep water resurfaces, balancing the deep water formations in North Atlantic and in the vicinity of Antarctic ice shelf, and in that it acts to connect the world's other oceans. The Southern Ocean is also regarded as a key region that draws large amount of C_{ANT} from the atmosphere and transports it to other ocean basins [e.g., *Caldeira and Duffy*, 2000].

The main water masses in the Southern Oceans are presented below. In their detailed discussions, it can be seen that the mid-latitude westerly winds (and the general wind fields in the Southern Ocean) plays a very important role in the formation and dynamic of these water-masses.

Circumpolar Deep Water (CDW)

CDW is an upwelled water mass found in the deeper part of the Southern Ocean. It is a result of different deep-water masses from other basins (the Pacific Deep Water, PDW, the Indian Ocean Deep Water, IDW, and North Atlantic Deep Water, NADW) mixing with the Antarctic Bottom Water (AABW). At around 60°S, as mid-latitude westerly winds transitions into polar easterlies towards the south, Ekman suction draws CDW up to within 200m of the surface. Its lighter component, the Upper Circumpolar Deep Water (UCDW), is mostly comprised of the PDW and IDW and can be identified by an oxygen minimum. It flows north after resurfacing and stays within the circumpolar structure of the ACC. In contrast, the denser component, the Lower Circumpolar Deep Water (LCDW), is mostly comprised of NADW and can be identified by a salinity maximum. Upon resurfacing, it flows south and enters subpolar regimes. This divide between Upper and Lower CDW are called the Antarctic Divergence in the earlier literature [e.g., *Tomczak and Godfrey*, 1994], but is referred by *Orsi et al.* [1995] as the *southern boundary of the ACC* (SB). This would be the term used by this thesis.

The wind-induced upwelling of UCDW is important to biological productivity in bringing nutrients back to the euphotic zone [*Talley et al.*, 2011]. This upwelling also bring up old water that is low in C_{ANT} concentration [*Williams and Follows*, 2011].

The Antarctic Intermediate Water (AAIW), Subantarctic Mode Water (SAMW) and Subtropical Mode Water (STMW)

These water masses are downwelled from the surface of the Southern Ocean. During late austral winter, the strong northward Ekman drift and relatively weaker Ekman pumping work in concert to subduct subantarctic water into the permanent thermocline as a thick, low potential-vorticity body of water [*Hanawa and Talley*, 2001]. The subduction region of SAMW is north of the Subantarctic Front (SAF), where a fast, narrow jet of the ACC is located, up to the Subtropical Front, where a sharp TS gradient marks the northern limit of circumpolar regimes [see *Orsi et al.*, 1995, for detailed fronts description]. STMW is less dense than SAMW and is associated with subtropical gyres further north. It is either formed from western boundary current extensions of subtropical gyres, or in its subduction areas [*Hanawa and Talley*, 2001]. The AAIW is formed from the densest part of SAMW in southeast South Pacific and southwest South Atlantic [e.g., *McCartney*, 1977; *England et al.*, 1993].

The subduction of SAMW is important in bringing oxygen to the subtropical pycnocline. In their formations, the AAIW and SAMW also take up large amounts of anthropogenic carbon from the atmosphere and transport it downward [*Sabine et al.*, 2004].

Southern Ocean ventilation plays a crucial role both on the regional and global scales. Any change the Southern-Ocean ventilation will therefore affect the global carbon budget, with important implications for the global climate.

1.2.2 Anthropogenic carbon in the ocean

Since the Industrial Revolutions in the mid-18th Century, human activities such as the burning of fossil fuels, cement production and deforestation have

released excessive carbon dioxide into the atmosphere, which is termed *anthropogenic* ('man-made') carbon, or C_{ANT} . This rise in C_{ANT} is partially absorbed by terrestrial biosphere as well as by the ocean. It is estimated the ocean has absorbed $\sim 40\%$ of total C_{ANT} ever released into the atmosphere [e.g., *Ciais et al.*, 2014].

The oceanic interior concentration of C_{ANT} is the increase in the dissolved inorganic carbon (DIC) attributable to the atmospheric CO₂ increase since the industrial revolution (~ 1750). C_{ANT} is not a directly measurable quantity for several reasons: Firstly, C_{ANT} is identified by its origin and is physically and chemically indistinguishable from natural DIC. Secondly, the inhomogeneous distribution of DIC and its variability due to complex ocean biogeochemistry tends to mask C_{ANT} signals. Therefore different indirect methods are necessary to quantify C_{ANT} in the ocean, each with its own innovations and challenges:

One type of approach utilizes local properties of water and their relationship with DIC to infer and remove the natural DIC concentration. The first type of them are back-calculation methods originally proposed by *Brewer* [1978] and *Chen and Millero* [1979]. Through various stages of improvement, the ΔC^* method of *Gruber et al.* [1996] is presently the most well-known in this group. The widely-used estimate of global C_{ANT} inventory by *Sabine and Gruber* [2005] is calculated using this ΔC^* method. Back-calculation methods are based on carbon chemistry in the ocean and uses oxygen, alkalinity and/or nutrients to remove pre-industrial DIC and DIC changes due to remineralization of organic matter and carbonate cycles. They are reliant the assumption of constant stoichiometric ratios between DIC and other tracers, which is not well met in shorter timescales and in some regions of the ocean [*Levine et al.*, 2008]. Other sources of bias includes the assumption of constant air-sea DIC disequilibrium, neglect of mixing when estimating water-mass age from CFCs and subjectivity when identifying end-member water types [*Matsumoto and*

Gruber, 2005]. Another more recent type is the purely empirical multiple linear regression (MLR) method [*Wallace*, 1995] which infers the background DIC by regressing measured DIC against other physical and biogeochemical tracers at one observation time. The underlying assumption is that the relationship between the background DIC and other tracers does not change with time, so the difference between the fitted and the observed DIC at a second time period can be ascribed to anthropogenic change. This method was then improved by *Friis et al.* [2005] to become extended MLR (eMLR) method. The eMLR method is used by, for example, *Wanninkhof et al.* [2010] on Section A16 to infer a decadal storage change of $0.53 \pm 0.05 \text{ mol m}^{-2}\text{yr}^{-1}$ in the Atlantic Ocean.

A second type of approach does not make use of measured DIC data. Instead, by treating the small anthropogenic perturbation over the background DIC as essentially a passive tracer, this type of studies infers surface-to-interior transport from observed tracers such as potential temperature, salinity, CFCs and radiocarbon, then uses the inferred transport to propagate the atmospheric CO₂ increase since the industrial revolution into the ocean interior. These methods avoid the challenges in separating C_{ANT} from background DIC and usually better address the role of mixing in C_{ANT} propagation. On the other hand, these studies need to contend with the uncertainty due to limited constraints on the transport provided by available tracers as well as the approximations needed for the air-sea CO₂ disequilibrium. The TTD method used by *Waugh et al.* [2004] and *Steinfeldt et al.* [2009] and the Green's function method used by *Khatiwala et al.* [2009] are examples of this type.

CHAPTER 2

Methods

2.1 Previous work

Earlier studies on ventilation timescales using tracers utilized the 'tracer age' of difference tracers such as CFCs and tritium [e.g., *Fine*, 1995], which is defined as the time lag between surface and interior tracer concentration. However, tracer ages have been shown to be a tracer-dependent property rather than intrinsic property of the flow [*Waugh et al.*, 2003]. *Holzer and Hall* [2000] gave a more physically sound framework by identifying the tracer-independent boundary propagator \mathcal{G} (called G' in their work). It is the Green's function of an advection-diffusion problem (for general settings, applicable in the ocean) with zero sources/sinks and specified mixing ratio at the boundary, and it acts with the mixed layer tracer concentration to propagate tracer into the interior.

Another challenge faced by studies of ocean ventilation using tracers is the high degree of uncertainty in view of limited tracer constraints available. Earlier methods [e.g., OMP method, *Tomczak and Large*, 1989] required investigators to first narrow down ventilation regions into a small number of alternatives (so-called endmembers). However, the Maximum Entropy framework [*Jaynes*, 1957] provides a powerful way of dealing with such uncertainty. *Primeau and Kibler* [2008] first applied this to World Ocean Atlas 2005 (WOA05) data to study climatological ventilation locations. *Khatiwala et al.* [2012] obtained ventilation timescale information by using transient tracers (radiocarbon and CFCs) in addition to WOA05. *Holzer et al.* [2010], the direct predecessor of

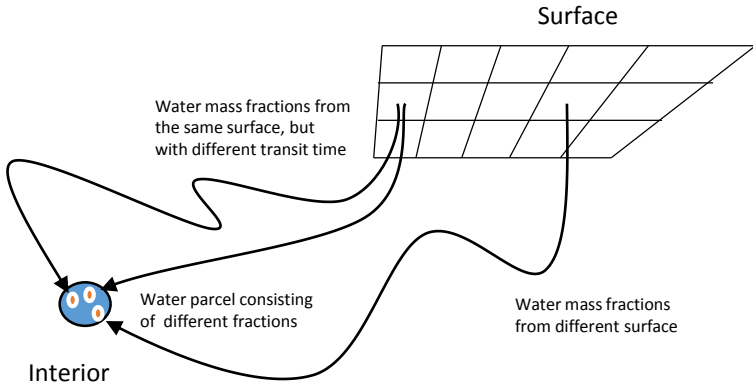


Figure 2.1: Schematic showing the different ventilation locations and transit times of ocean transport.

this study, further included the high-quality WOCE A20 hydrography data to study North Atlantic ocean in greater interior resolution. It used two repeat hydrography datasets, separated by 6 years, to constrain the boundary propagator, assuming steady transport during this period. Our study uses repeat hydrography data that is about 15 years apart (from around 1992 to around 2007) to study the decadal changes in the transport, rather than the climatology (We note that *Holzer et al.* [2010] also did use repeat hydrography, but with assumption of stationary transport between the years of data obtained so the transport information is more of climatology). In contrast, we do not invoke such an assumption, and was able to obtain the state of the transport separately. Our study also has higher resolution for the surface ventilation location grid boxes ($3^\circ \times 3^\circ$ in contrast to $5^\circ \times 5^\circ$ of *Holzer et al.* [2010] or 26 coarse surface patches of *Khatiwala et al.* [2012]).

2.2 The boundary propagator \mathcal{G}

In the absence of mixing, a water parcel would stay intact as it makes its journey from the surface into the interior. That means every water parcel found in the interior position \mathbf{r} and time t can be linked to a single surface source at a single time point in the past. In reality, however, as a water parcel leaves the surface, it is subject to mixing processes of various scale, so that

at any location in the interior, we find that the water parcels are actually a mixture of different surface sources \mathbf{r}_s with different transit times (or age) τ .

The boundary propagator

$$\mathcal{G}(\mathbf{r}, t; \mathbf{r}_s, \tau) \quad (2.1)$$

physically represents the (per unit area and transit time) fraction of the water-mass found in the interior point \mathbf{r} at time t that was last ventilated at the surface patch $\mathbf{r}_s d^2 r_s$, during the interval $[t - \tau, t - (\tau + d\tau)]$.

Conservative tracers in the ocean are valuable in giving us insights into the ocean transport. Before the theoretical framework of TTD or \mathcal{G} was in place, the age of a water parcel was defined to be the elapsed time since a particular tracer's surface concentration was equal to its interior concentration (termed the *tracer age*), and was widely applied on transient tracers such as CFCs and tritium [e.g. *Fine*, 1995]. However, it was found that different tracers produce different tracer ages. *Hall and Plumb* [1994] showed that the tracer ages are dependent on the shape of the tracer surface concentration history and only really reflect the time since last ventilation in special cases. Subsequently, *Holzer and Hall* [2000] and *Haine and Hall* [2002] suggested that the transport information encoded in tracers should be interpreted in the following way: That the interior concentration $C^I(\mathbf{r}, t)$ of a tracer at time t and interior point \mathbf{r} is related to its surface concentration history $C^S(\mathbf{r}_s, t - \tau)$, which spans all surface points \mathbf{r}_s and all past time $t - \tau, \tau > 0$, via a convolution with an integration kernel, i.e.,

$$C^I(\mathbf{r}, t) = \int d^2 r_s \int_0^\infty d\tau \mathcal{G}(\mathbf{r}, t; \mathbf{r}_s, \tau) C^S(\mathbf{r}_s, t - \tau), \quad (2.2)$$

where the integration kernel \mathcal{G} is the boundary propagator. For radioactive tracers such as ^{14}C , a decay term $e^{-\tau/T}$ is added to the integrand, where T is the e -folding decay timescale. The contribution of $C^S(\mathbf{r}_s, t - \tau)$ to $C^I(\mathbf{r}, t)$ is weighted by \mathcal{G} .

It is remarkable that the boundary propagator \mathcal{G} has a deeper meaning. In the partial differential equation setting, $\mathcal{G}(\mathbf{r}, t; \mathbf{r}_s, \tau)$ is in fact the Green's function to the ocean advection-diffusion equation with a single source impulse at point \mathbf{r}_s surface boundary at time $t - \tau$, in the absence of interior source and sink. It contains the same transport information as the advection-diffusion differential operator. However, if one would like to examine the distribution of a certain tracer given its surface history (as we do in this case, to study C_{ANT}), the boundary propagator readily computes it via a convolution, rather than via time-marching algorithms required by its differential counterpart. This advantage in fact motivated the term ‘boundary propagator’.

The quest then lies with first finding the boundary propagator. Given available interior tracer snapshot at a point \mathbf{r}, t and surface history for all \mathbf{r}_s and $\tau > 0$, we can then use (2.2) to deconvolve for the boundary propagator at that \mathbf{r}, t .

2.3 The principle of Maximum Entropy (ME)

One immediate challenge when using the boundary propagator framework is the sparsity of available constraints to specify the propagator. Tracers that are suitable to act as constraints need to (1) be conservative, or have simple sources or sinks, e.g., sink in a form of radioactive decay, (2) be practically measurable in the ocean interior, and (3) have a surface history available to us. The third criterion is by far the hardest to be met and assumptions about the surface history have to be made. There are thus but a handful of tracer that meet the remaining two criteria. Hence, given available constraints, a multitude of feasible \mathcal{G} exist, i.e., they can propagate the surface tracer history to match the observed interior concentration. We then ask the question: Which one is the most sensible choice?

To understand the principle maximum entropy (ME), we need the concept of information entropy, as developed by *Shannon* [2001]. For any discrete

probability distribution p_i , we can uniquely and unambiguously quantify its *amount of uncertainty* as, to within a multiplicative constant K ,

$$H = -K \sum_i p_i \log p_i. \quad (2.3)$$

This quantity has zero as the minimum when the probability is unity for a certain i entry and zero elsewhere¹, and attains maximum when the probability is uniformly distributed across all i 's. This quantity agrees with our intuitive notion that a spread-out distribution represents more uncertainty, or has less information specified, than a sharply peaked distribution. The $x \log x$ form of the information entropy implicitly bounds the probabilities away from zero and hence negative values.

The ME principle utilizes this property in its choice of \mathcal{G} . Returning to the previous problem, one ‘natural’ rationale is to choose a least biased \mathcal{G} on the given constraints - one that best reflects our current knowledge (or rather, the current *lack* of knowledge) of the transport. So subject to all the given constraints, we seek a \mathcal{G} , out of all plausible ones, that represents the most uncertainty, since choosing any other \mathcal{G} amounts to specifying arbitrary features unsubstantiated by data. This ME \mathcal{G} may not be the one closest to the real transport - we have no way of knowing whether or not that is the case - but it is the best one we can produce given the currently available information. To do any better, we would need more information that can be obtained by extra constraints, for example.

We now present our formulation of the maximum entropy method, beginning with discretization of the boundary propagator². Let $\mathcal{G}(\mathbf{r}_s, \tau)$ be the boundary propagator that is defined for an interior location \mathbf{r} and time t .

¹Using the definition $0 \log 0 \equiv \lim_{x \rightarrow 0^+} x \log x = 0$.

²Although the information entropy can be defined for continuous distributions [Jaynes, 1963], our hydrographic data sampled at discrete time and location makes it more practical to apply the ME methods to a discretized \mathcal{G} .

Real world application requires it to be discretized both in the surface location \mathbf{r}_s and transit time τ . Let the surface locations be partitioned into (not necessarily equal) areas indexed by $s = 1, \dots, S$, and the transit time years be specified in a finite length (and not necessarily equally spaced) vector of nodes $\tau_y(n), n = 1, \dots, N$, where $\tau_y(N)$ is the maximum transit time reasonably chosen for numerical computation. Also, let every year be subdivided into equal intervals indexed by $m = 1, \dots, M$ to approximate months ($M = 12$) or seasons ($M = 4$). Under such a scheme, we define the discretized boundary propagator to be the integral of \mathcal{G} over the a surface patch for the selected month and year interval, i.e.,

$$\mathcal{P}(m, n, s) \equiv \int_{\mathbf{r}_s \in \Omega_s} d^2 r_s \left[\frac{m-1}{M} \leq \tau_{m,n} - \lfloor \tau_{m,n} \rfloor \right] \mathcal{G}(\mathbf{r}_s, \tau_{m,n}) \quad (2.4)$$

where $[\cdot]$ is the Iverson bracket and

$$\tau_{m,n} \equiv \tau(n) + \frac{m}{M}. \quad (2.5)$$

Note that this definition preserves the continuous nature of the transit time year, since in practice the transit time year component is usually integrated over using numerical quadrature, whereas the transit time seasons/months and surface locations are simply summed over. Appendix A.1 contains details about the time and spatial discretization used in our study.

Apart from the tracer constraints, we usually have some prior knowledge about the features of the boundary propagator. The ME approach allows for the incorporation of such prior knowledge about distribution of surface ventilation locations and transit times. Given a prior, maximizing the information entropy then ‘updates’ the distribution with the information contained within

the tracer constraints. After applying similar discretization to the prior to obtain $\mu(m, n, s)$, we incorporate the information from the J tracer constraints by solving the following optimization problem[Press, 2007]:

$$\text{maximize } \mathcal{S} \equiv - \sum_{m,n,s} w_n \mathcal{P} \log \frac{\mathcal{P}}{\mu} \quad (2.6)$$

with respect to $\mathcal{P}(m, n, s)$ at every discrete point (m, n, s) , subject to

$$\sum_{m,n,s} w_n \mathcal{P} = 1 \quad (2.7)$$

$$\sum_{m,n,s} w_n \mathcal{P} C_j^S = C_j^I \quad \text{for } j = 1, \dots, J, \quad (2.8)$$

where w_n is the weight in the numerical quadrature over transit time, associated with the year vector τ_y .

Using the method of Lagrange multipliers, we obtain the maximum entropy solution

$$\hat{\mathcal{P}} = \frac{1}{Z} \mu(m, n, s) \exp \left(- \sum_{j=1}^J \lambda_j C_j^S(m, n, s) \right), \quad (2.9)$$

where $Z \equiv \sum_{m,n,s} \mu(m, n, s) \exp \left(- \sum_{j=1}^J \lambda_j C_j^S(m, n, s) \right)$ normalizes the distribution. The λ_j are J Lagrange multipliers and are then found numerically using the J constraints (2.8) with $\hat{\mathcal{P}}$ in place of \mathcal{P} . Appendix A describes in detail the set up of the numerical method in MATLAB.

In the following example, we illustrate the details in finding $\hat{\mathcal{P}}$ for simple $J = 1$ case.

Example 2.3.1. For the case $J = 1$, i.e., only one tracer constraint is available, we seek to maximize $\mathcal{S} \equiv - \sum_{m,n,s} w_n \mathcal{P} \log \frac{\mathcal{P}}{\mu}$ with respect to $\mathcal{P}(m, n, s)$ at

every discrete point (m, n, s) subject to

$$\sum_{m,n,s} w_n \mathcal{P} = 1 \quad (2.10)$$

$$\sum_{m,n,s} w_n \mathcal{P} C_1^S = C_1^I \quad (2.11)$$

Since all the $P(m, n, s)$ are independent of each other, for all (m', n', s') in the discrete domain, we have, by the method of Lagrange multipliers,

$$\begin{aligned} \partial_{P(m', n', s')} \mathcal{S} &= \lambda_1 \partial_{P(m', n', s')} \left(\sum_{m,n,s} w_n \mathcal{P} C_1^S - C_1^I \right) \\ &\quad + \lambda_0 \partial_{P(m', n', s')} \left(\sum_{m,n,s} w_n \mathcal{P} - 1 \right). \end{aligned} \quad (2.12)$$

All but the $\mathcal{P}(m', n', s')$ terms vanish in the summations to give

$$-\left(\ln \frac{\mathcal{P}(m', n', s')}{\mu(m', n', s')} + 1 \right) = \lambda_1 C_1^S(m', n', s') + \lambda_0 \quad (2.13)$$

Therefore

$$\mathcal{P}(m', n', s') = \mu(m', n', s') \exp(-\lambda_1 C_1^S(m', n', s')) e^{1-\lambda_0}, \text{ and} \quad (2.14)$$

$$\mathcal{P}(m, n, s) = \mu(m, n, s) \exp(-\lambda_1 C_1^S(m, n, s)) e^{1-\lambda_0} \quad (2.15)$$

We shall now enforce the constraint (2.7) on (2.15), giving

$$1 = e^{1-\lambda_0} \sum_{m,n,s} w_n \mu(m, n, s) \exp(-\lambda_1 C_1^S(m, n, s)),$$

which is satisfied by setting $e^{1-\lambda_0} = \left(\sum_{m,n,s} w_n \mu(m, n, s) \exp(-\lambda_1 C_1^S(m, n, s)) \right)^{-1} \equiv \frac{1}{Z_1}$, so we arrive at

$$\hat{\mathcal{P}}_1 = \frac{1}{Z_1} \mu \exp(-\lambda_1 C_1^S). \quad (2.16)$$

It then remains to substitute $\hat{\mathcal{P}}_1$ into (2.11) to solve for λ_1 numerically.

Jaynes [1963] demonstrated in a short proof that this ME solution, if it exists, is unique over all m, n, s . Any other distinct \mathcal{P} s would have smaller entropy. We here present a result that this translates to a unique set of λ_j subject to certain conditions on C_j^S .

Proposition 2.3.2. *[Uniqueness of Lagrange multipliers] For a deconvolution problem with linearly-independent (in J dimension) and centered (i.e., $\sum_{m,n,s} C_j^S = 0$ for all j) C_j^S , if a ME solution exists, the set of Lagrange multipliers is unique for a fixed prior μ and set of C_j^I .*

Proof. For the ME solution in 2.9, suppose there is another ME solution, *Jaynes* [1963] tells us that it would be still of the form $\frac{1}{Z'} \mu \exp(-\sum_j \lambda'_j C_j^S)$ and is identically equal to $\hat{\mathcal{P}}$, although with perhaps different Z' and λ'_j . This means that for all m, n, s ,

$$\exp\left(-\sum_j \lambda_j C_j^S(m, n, s)\right) = \alpha \exp\left(-\sum_j \lambda'_j C_j^S(m, n, s)\right) \quad (2.17)$$

for some $\alpha \equiv Z/Z' > 0$. Taking the logarithm of both sides gives

$$\begin{aligned} -\sum_j \lambda_j C_j^S &= \log \alpha - \sum_j \lambda'_j C_j^S \\ \sum_j (\lambda'_j - \lambda_j) C_j^S &= \log \alpha. \end{aligned} \quad (2.18)$$

If we now define $\lambda, \lambda' \in \mathbb{R}^{J \times 1}$ to be column vectors of λ_j, λ'_j and ones respectively, and $C \in \mathbb{R}^{MNS \times J}$ be a matrix with rows of C_j^S , (2.18) can be

written as the matrix equation

$$C(\lambda' - \lambda) = \log \alpha \cdot \mathbf{1}. \quad (2.19)$$

We can multiply both sides by C^T to give

$$C^T C (\lambda' - \lambda) = \log \alpha \cdot C^T \mathbf{1} = \mathbf{0} \quad (2.20)$$

since the C_j^S are centered. Then, since C_j^S are linearly-independent, $C^T C$ has full rank and is hence invertible, and we have the result $\lambda' - \lambda = \mathbf{0}$. That is, $\lambda'_j = \lambda_j$ for all j . \square

If C_j^S is not centered for some j , one can always center it and apply the same offset to C_j^I , before performing the deconvolution.

One feature that any consistent inference principle should have is the invariance of the solution under changes in the order and time of the application of the information. In another word, suppose one has a number of constraints available, one should arrive at the same solution regardless of whether the constraints are applied simultaneously or one at a time (with solutions at each iteration retained to be the prior of the next) and regardless of the order of applying the constraints. We here show that the principle of maximum entropy has this property.

Example 2.3.3. Suppose that, following Example 2.3.1, a new constraint is available as

$$\sum_{m,n,s} w_n \mathcal{P} C_2^S = C_2^I, \quad (2.21)$$

where C_2^S is linearly-independent to C_1^S . If we choose to use the previous solution (i.e., (2.16), with λ_1 already determined) as a prior, then our entropy

formulation becomes

$$\mathcal{S} = \mathcal{P} \log \frac{\mathcal{P}}{\hat{\mathcal{P}}_1}. \quad (2.22)$$

Maximizing this subject to (2.7) and (2.21), analogous to Example2.3.1, yields

$$\begin{aligned} \mathcal{P}(m, n, s) &= \hat{\mathcal{P}}_1(m, n, s) \exp\left(-\lambda_2 C_2^S(m, n, s)\right) e^{1-\lambda'_0} \\ &= \frac{e^{1-\lambda'_0}}{Z_1} \mu(m, n, s) \exp\left(-\lambda_1 C_1^S(m, n, s) - \lambda_2 C_2^S(m, n, s)\right) \end{aligned} \quad (2.23)$$

with λ_2 and λ'_0 being the new Lagrange multipliers. We again enforce (2.7) on (2.23) by setting $e^{1-\lambda'_0}/Z_1 = (\sum_{m,n,s} w_n \mu \exp(-\lambda_1 C_1^S - \lambda_2 C_2^S))^{-1} \equiv 1/Z_2$.

Finally we arrive at

$$\hat{\mathcal{P}}_2 = \frac{1}{Z_2} \mu \exp\left(-\lambda_1 C_1^S - \lambda_2 C_2^S\right) \quad (2.24)$$

and numerical solver will give us λ_2 that satisfies (2.21).

Note that if we have (2.11) and (2.21) both available and apply them simultaneously, we would arrive at exactly the same solution form. If we should have (2.21) available to us before (2.11), it is easily seen that we would still arrive at the same solution form. By Proposition2.3.2, these all yield the same ME solution with the same λ_1 and λ_2 . This shows the Bayesian nature of how information from the constraints are handled by the principle of maximum entropy.

One ramification of this property is that, after we performed inference on \mathcal{G} using the currently available data, should more constraints become available to us in the future, we can take our current maximum entropy solution as the prior and solve for a new solution subject to just the additional constraints.

CHAPTER 3

Data

Here we describe the data relevant to our problem of quantifying the decadal change. Where the details are more computational, the descriptions are deferred to A.

We utilize the following tracers that are conserved or decays with a known rate: conservative temperature Θ , absolute salinity S_A , PO_4^* (a quasi-conserved tracer, defined by $\text{PO}_4^* \equiv \text{PO}_4 + \text{O}_2/175$, used by e.g., Broecker *et al.* [1998]), CFC-11 and CFC-12, and natural (pre-bomb) $\Delta^{14}\text{C}$. Our Θ and S_A are derived from pressure, *in situ* temperature, practical salinity and longitude, latitude of the data using the Gibbs-Sea Water (GSW) Oceanographic Toolbox [McDougall and Barker, 2001].

3.1 Surface history data

Our Θ , S_A and PO_4^* surface history are derived from the World Ocean Atlas 2009 temperature, salinity, oxygen and nutrients climatology [Locarnini *et al.*, 2010; Antonov *et al.*, 2010; Garcia *et al.*, 2010a, b]. The climatological data specifies a fine spatial distribution as well as monthly cycles, but not the interannual and longer timescale variability. Due to insufficient knowledge on their changes, we invoke the cyclostationary assumption (i.e., no interannual trend and the seasonal cycle repeats itself every year). The information on interannual and longer timescale variability is instead provided by the natural (pre-bomb) $\Delta^{14}\text{C}$, CFC-11 and CFC-12 tracers. The spatial distribution of both tracers are available as annual climatological mean from the Global Ocean

Data Analysis Project (GLODAP) data set *Key et al.* [2004]. The radiocarbon history is assumed to be roughly constant in time. Exploiting the short equilibration time of CFCs into the surface mixed layer, we incorporate the year dependence by identifying the nominal year of the CFC-11 and CFC-12 surface climatology to be $y_{GLODAP} = 1988$ (see Appendix B for the methods used to determine y_{GLODAP}), and scale it by the ratio $\text{CFC}(y_n)_A/\text{CFC}(y_{GLODAP})_A$, where $\text{CFC}(y_n)_A$ is the measured global annual mean atmospheric concentration for year y_n [*Walker et al.*, 2000]. Because of the cyclostationary assumption, we restrict our studies to depth below 250m, where it is less susceptible to interannual variations, which have the potential to obscure the decadal changes we seek to quantify.

3.2 Interior Data

There are several high-quality hydrography lines in the Southern Ocean that have two repeat observations that are 12 years or longer apart. To thoroughly examine the decadal changes in the Southern Ocean, we took one line from the Atlantic basin (A16), two from the Pacific basin (P16 and P18), one from the Indian basin (I8S and I9N forming one line) and one south of Australia (S3). Table 3.1 lists the hydrography lines used in our analysis. Θ , S_A , PO_4^* and CFCs concentrations are all obtained or derived from the bottle measurements. To ensure data quality, bottles flagged to have questionable quality are discarded. We could not make use of the radiocarbon measurement from the hydroographies, as testing of nuclear weapons in the late 1950s and early 1960s introduced a large and transient feature in surface radiocarbon concentration (the 'bomb spike') whose history is not yet available to us. We instead use the climatological natural carbon measurement from GLODAP as our interior data. We interpolate the natural $\Delta^{14}\text{C}$ at the bottle locations from the GLODAP gridded interior data. All hydrography data sections are gridded before deconvolution.

Line	Date collected	Nominal year & month	Time between observations
P16	12 Aug 1991 - 25 Aug 1991	Sep 1992	12y5m
	12 Oct 1992 - 28 Oct 1992		
P18	11 Jan 2005 - 11 Feb 2005	Feb 2005	12y10m
	27 Feb 1994 - 25 Apr 1994	Mar 1994	
A16	17 Dec 2006 - 14 Feb 2007	Jan 2007	15y11m
	1 Feb 1989 - 17 Feb 1989	Mar 1989	
	21 Mar 1989 - 8 Apr 1989		
I8S/I9N	17 Jan 2005 - 21 Feb 2005	Feb 2005	12y3m
	I8S: 19 Dec 1994 - 28 Dec 1994	Jan 1995	
	I9N: 28 Jan 1995 - 24 Feb 1995		
	I8S: 16 Feb 2007 - 12 Mar 2007	Apr 2007	
S3	I9N: 26 Mar 2007 - 27 Apr 2007		16y6m
	8 Oct 1911 - 26 Oct 1911	Oct 1991	
	23 Mar 2008 - 15 Apr 2008	Apr 2008	

Table 3.1: Hydrography lines used in this study.

3.3 C_{ANT} data

The inorganic carbonate chemistry system [Sarmiento, 2013] has been used to calculate DIC concentration boundary conditions from GLODAP total Alkalinity, and WOA09 temperature and practical salinity. This provides a $1^\circ \times 1^\circ$ DIC field (which is then interpolated to our $3^\circ \times 3^\circ$ grid) for every year from 1720 to 2012 based on chemical equilibrium with the atmospheric partial pressure of CO₂ (pCO₂). To cover the 18th century, the Goddard Institute for Space Studies (GISS) data set of observed atmospheric pCO₂ from 1850 to present was extended back to 1720 using ice-core data from the CDIAC (Carbon Dioxide Information Analysis Centre) archive (<http://data.giss.nasa.gov/modelforce/ghgases>, <http://cdiac.ornl.gov>). The pCO₂ air-sea disequilibrium has been assumed to be constant in time and was estimated from the GLODAP DIC dataset for the nominal GLODAP year of 1994. (http://cdiac.ornl.gov/oceans/glodap/data_files.html).

3.4 Choice of Prior

We use a prior derived from the data-assimilated, steady circulation model used in *Primeau et al.* [2013], which is an improved version of *DeVries and Primeau* [2011]. The model is $2^\circ \times 2^\circ$ with 24 vertical levels, with thickness ranging from 30 m at the surface to 650 m in the deepest layer. The steady circulation is maintained by the global climatological wind stress field of *Trenberth et al.* [1989], with specified horizontal and vertical viscosity of $A_h = 5 \times 10^4 \text{ m}^2\text{s}^{-1}$ and $A_v = 10^{-4} \text{ m}^2\text{s}^{-1}$, and is constrained by temperature, salinity, phosphate, CFC-11 and radiocarbon. The circulation's advective-diffusive transport operator has fixed horizontal and vertical eddy diffusivities of 10^3 and $10^{-5} \text{ m}^2\text{s}^{-1}$, respectively, typical of coarse-resolution models. The model's Atlantic meridional overturning circulation and meridional heat and freshwater fluxes were accessed for realism at $4^\circ \times 4^\circ$ resolution in *DeVries and Primeau* [2011]. The model's ability to capture transport in AABW, AAIW, SAMW, and NADW was quantified in terms of water mass fractions in *DeVries and Primeau* [2011] and, at $2^\circ \times 2^\circ$ resolution, in terms of the ability to simulate the observed distribution of CFC-12 in the Southern Ocean in *Waugh et al.* [2013].

For every interior point \mathbf{r}' in this model grid, we extract transport information in the form of water-mass fractions $f_M(\mathbf{r}'; l)$ last ventilated in 14 patches Ω_l that partition the global ocean surface, and their respective mean transit time $\Gamma_M(\mathbf{r}'; l)$ since last ventilation, where $l = 1, 2, \dots, 14$ labels the patches. These f_M and Γ_M are then interpolated onto our grid, and the full prior μ is given by

$$\mu(\mathbf{r}; m, n, s) = \sum_{l=1}^{14} \mathbf{I}_{\Omega_l \ni s} f_M(\mathbf{r}; l) g_{IG}(\tau_{m,n}; \Gamma_M(\mathbf{r}; l)) \quad (3.1)$$

where $g_{IG}(\tau, \Gamma)$ is an inverse Gaussian distribution of the transit time τ , with Γ as the mean parameter and a Péclet number of 1, suitable as a prior guess at typical ocean values [*Waugh et al.*, 2004].

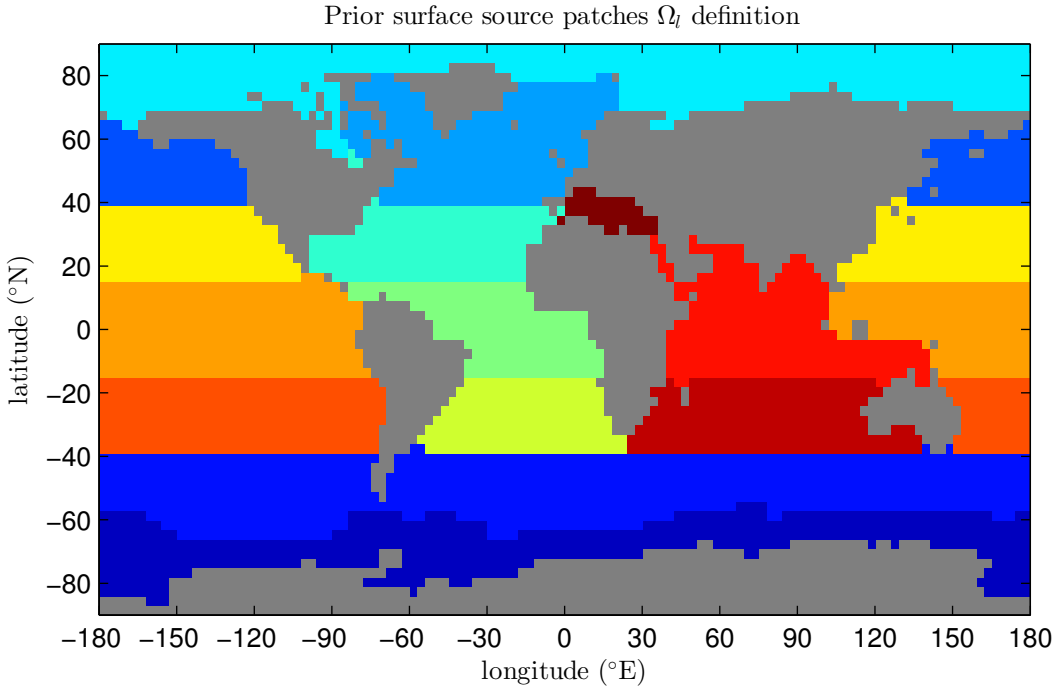


Figure 3.1: Surface regions Ω_i 's definition used in prior.

The surface patch definition used for the prior is given in Figure 3.1. The 14 patch-integrated f_M and Γ_M are used instead of the full model output so as to avoid building excessive model product into our deconvolution.

3.5 Uncertainly estimation

We want to note that our current variation of the ME method enforces exact fit to the tracer data, and essentially assumes zero errors in the measurement. However, taking the data error into account would render our problem into a large scale optimization problem, and since *Holzer et al.* [2010] reported that the data error is typically much smaller than the uncertainty inherent to solving our inverse problems with few constraints, we elect not to quantitatively study the effect of this type of error to our solution. However, we have examined the error due to the sparsity of our data by examining the sensitivity of our solution to uncertainties in our prior information μ . A detailed description of the prior perturbation setup can be found in Section A.4.

CHAPTER 4

Results

4.1 The Boundary Propagator \mathcal{G}

We can summarize the information on ventilation location and transit time contained in \mathcal{G} by computing its key moments. For each of these moments, we first present its estimate at time t_1 of original measurement, followed by the change per decade estimated from the $t_2 - t_1$ difference.

We note that in the literature, SAMW and STMW are identified in terms of potential vorticity minima [Hanawa and Talley, 2001], AAIW in terms of salinity minimum, UCDW as an oxygen minimum, and UCDW as an salinity maximum [Orsi *et al.*, 1995]. For these water masses, we define σ_0 potential density bounds that mostly capture these property extrema. The bounds are as given in Table 4.1 and we will use these σ_0 -based definitions for the water masses throughout our analysis. Note that we preserve the original overlapping definition of the water masses for ease of comparison with other studies.

Water-mass name	Definition (σ_0 in kg m^{-3})
Subtropical Mode Water (STMW)	$\sigma_0 \leq 26.6$, south of 10°S
Subantarctic Mode Water (SAMW)	$26.6 \leq \sigma_0 \leq 27.2$
Antarctic Intermediate Water (AAIW)	$27 \leq \sigma_0 \leq 27.6$
Upper Circumpolar Deep Water (UCDW)	$27.2 \leq \sigma_0 \leq 27.8$, centered at $\sigma_0 = 27.6$
Lower Circumpolar Deep Water (LCDW)	$\sigma_0 \geq 27.6$, centered at $\sigma_0 = 27.8$

Table 4.1: Definitions of the water-mass density classes used in this study.

4.1.1 Base state in early 1990s

Water-mass fractions older than τ^* years, f

We first look at the timescales of waters at time t_1 ('base state'). For any water parcel with interior location \mathbf{r} at observation time t , the fraction of water that was last ventilated more than τ^* years ago, regardless of where that last ventilation occurred, can be obtained from the boundary propagator as

$$f(\mathbf{r}, t; \tau^*) = \int d^2 r_s \int_{\tau^*}^{\infty} d\tau \mathcal{G}(\mathbf{r}, t; \mathbf{r}_s, \tau). \quad (4.1)$$

We refer to this as the global water-mass fraction older than τ^* . Note that its complement, $1 - f(\mathbf{r}, t; \tau^*)$, is the fraction of water that was last ventilated less than τ^* years ago, i.e., $1 - f(\mathbf{r}, t; \tau^*)$ is the global water-mass fraction younger than τ^* . The quantity $f(\mathbf{r}, t; \tau^*)$ is also the cumulative tail distribution of the global transit time distribution (TTD). That is,

$$f(\mathbf{r}, t; \tau^*) = \int_{\tau^*}^{\infty} d\tau g(\mathbf{r}, t; \tau), \quad (4.2)$$

where

$$g(\mathbf{r}, t; \tau) \equiv \int d^2 r_s \mathcal{G}(\mathbf{r}, t; \mathbf{r}_s, \tau), \quad (4.3)$$

is the water parcel's global TTD. However, as f is numerically more robust than g , we focus on f here.

We first examine the recently-ventilated waters. Figure 4.1a shows $f(\mathbf{r}, t_1; 30 \text{ yr})$. (The choice of the transit time year threshold $\tau^* = 30 \text{ yr}$ will be explained as we examine the decadal change in f in Subsection 4.1.2.) The complement of $f(\mathbf{r}, t_1; 30 \text{ yr})$ (i.e., the fraction younger than 30 yr) has a pattern similar to that of CFC's (Figure C.2 of Appendix C), that were introduced into the atmosphere only after ~ 1930 . This water-mass fraction younger than 30 yr

comprises most of STMW as well as the part of SAMW closest to its subduction zone, decreasing to $\sim 10\%$ by ~ 1500 m depth. Almost all of LCDW having been ventilated much more than 30 yr before t_1 .

Global mean transit time, Γ

We now examine the mean transit time of waters within the Southern Ocean since they were last ventilated. The mean transit time of water irrespective of ventilation region, Γ (which we call the global mean transit time¹) is defined to be the first moment of \mathcal{G} with respect to transit time τ after integrating over all possible surface ventilation locations, i.e.,

$$\Gamma(\mathbf{r}, t) \equiv \int d^2 r_s \int_0^\infty d\tau \tau \mathcal{G}(\mathbf{r}, t; \mathbf{r}_s, \tau) \quad (4.4)$$

$$= \int_0^\infty d\tau \tau g(\mathbf{r}, t; \tau) \quad (4.5)$$

Figure 4.1b shows the global mean age at t_1 along the five transects considered. We see that the global mean transit time ranges from the very young SAMW near the SAMW density outcrop to the very old deep waters in the tropics. Close to 60°S , the global mean transit time of LCDW is 400-500 years, showing that this is old upwelling water. For SAMW, $\Gamma(\mathbf{r}, t_1)$ starts by definition near zero close to the outcrop and exceeds 50 years by $\sim 30^\circ\text{S}$ after it subducts. AAIW is sandwiched between the old LCDW and the young SAMW and Γ have exhibited a smooth gradation across the water masses. In the topics, SAMW gradually mixes with deep water and becomes older to various extents depending on the ocean basin. There is a large difference in Γ between the deep waters of different basins. NADW in the Atlantic basin is as young as ~ 200 yr, while deep water in the Pacific and Indian Ocean is up to 1000yr old. This is expected from the vigorous overturning circulation of

¹Also known as the ideal mean age in literature.

the Atlantic and consistent with recent model analysis of the global ventilation paths [Primeau and Holzer, 2006; Holzer and Primeau, 2006]

TTD width, Δ

The width of the global TTD is defined in terms of the second temporal moment of g as

$$\Delta(\mathbf{r}, t) \equiv \sqrt{\frac{1}{2} \int_0^\infty d\tau (\tau - \Gamma(\mathbf{r}, t))^2 g(\mathbf{r}, t; \tau)}, \quad (4.6)$$

TTD width is a metric that quantifies the broadness of the transit time distribution and the width relative to the mean transit time is a proxy for the importance of mixing of waters with different paths to (\mathbf{r}, t) . Because Δ tends to increase with mean age, plotting Δ (not shown) reveals features highly similar to those of Γ . We therefore examine the ratio Δ/Γ at t_1 , plotted in Figure 4.1c.

We see that a ratio of Δ/Γ between 0.5–2 is ubiquitous in the Southern Ocean between 500–1500m depth. This range coincides with the ratio inferred by *Waugh et al.* [2004] for water in North Atlantic using a different method. However, Δ/Γ exceeds a value of 2 within STMW and in the upper 750m of AAIW, in vicinity of SAF and PF. This shows that STMW and AAIW are admixtures of waters with a wide spectrum of transit time since last ventilation. The larger Δ/Γ of AAIW may be a consequence of mesoscale eddies produced by the strong, meandering jets within SAF or PF, or may merely reflect the mixing of old CDW and young SAMW at their interface.

Water-mass fractions last ventilated in Ω_i , f_{Ω_i}

Because our tracer deconvolution allows us to extract information of last ventilation location, we further partition the water-mass fractions according to their last ventilation regions. By integrating \mathcal{G} over partial surface regions Ω_i ,

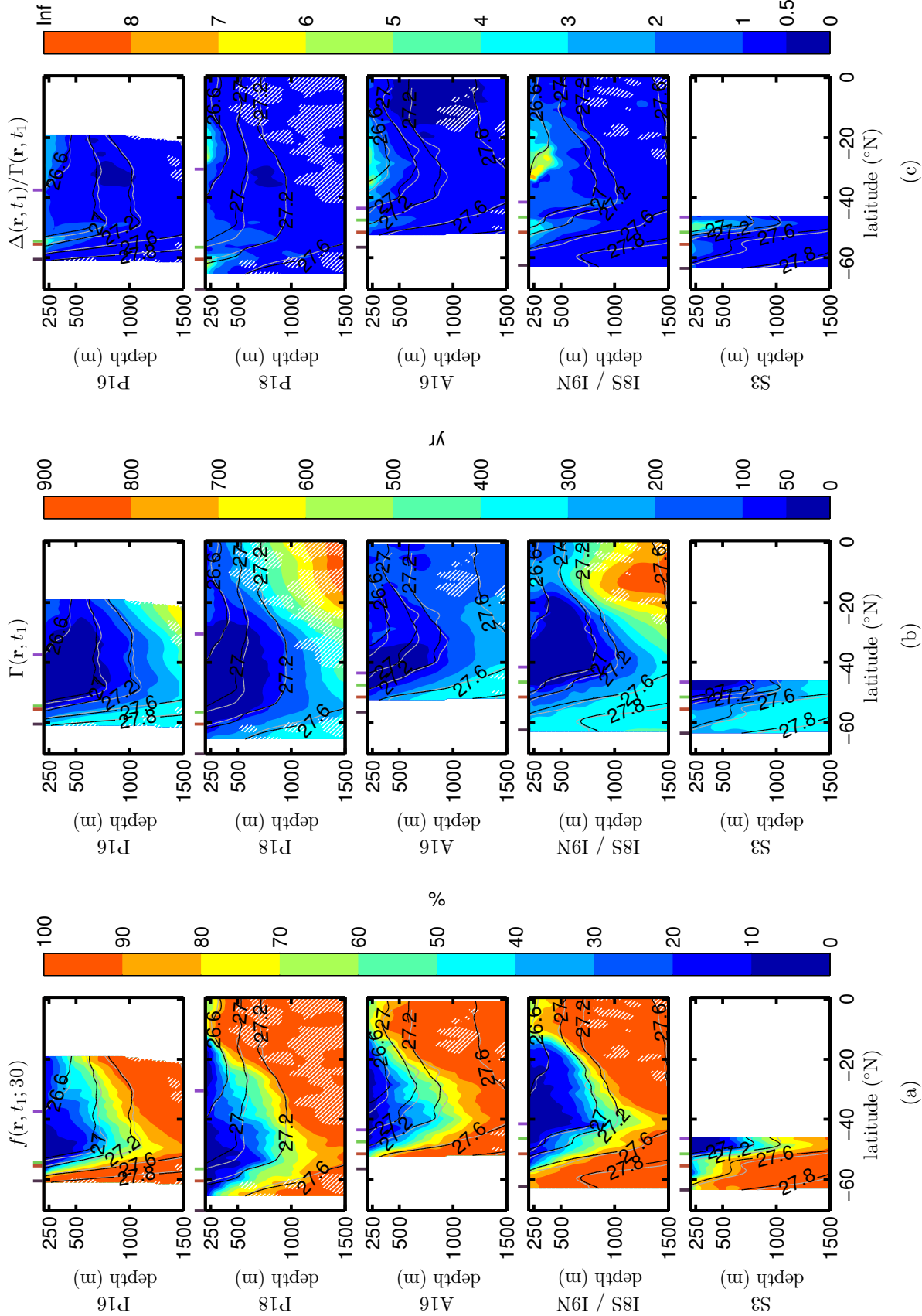


Figure 4.1: (a) Water mass fraction older than 30 yr at t_1 , irrespective of ventilation region. (b) global mean age of water at t_1 . (c) The ratio Δ/Γ at t_1 . Potential density anomaly contours for t_1 and t_2 are shown in black and grey, respectively. Interior locations where the deconvolution does not converge are hatched in white. The climatological fronts from Orsi *et al.* [1995] indicated by ticks on the top edge of all figures are: southern boundary of the ACC (SB, black), polar front (PF, brown), subantarctic front (SAF, green) and subtropical front (STF, purple). Same potential density anomaly contours and ticks are used in subsequent figures.

we obtain

$$f_{\Omega_i}(\mathbf{r}, t; \tau^*) = \int_{\Omega_i} d^2 r_s \int_{\tau^*}^{\infty} d\tau \mathcal{G}(\mathbf{r}, t; \mathbf{r}_s, \tau). \quad (4.7)$$

We partition the global ocean surface into key ventilation regions Ω_i 's, defined in Figure 4.2. Within the Southern Ocean, we have defined the region south of the Southern Boundary of the ACC (south of SB), the region between the Southern Boundary of the ACC and the Subantarctic Front (SB-SAF), and the region between SAF and the Subtropical Front (SAF-STF). Collectively, these three regions will be referred to as the Southern-Ocean fractions (SO). SB marks the boundary between the ACC and subpolar regimes while STF marks the boundary between the ACC and subtropical regimes [Orsi *et al.*, 1995]. Between the two boundaries, SAMW is found to form north of SAF [Hanawa and Talley, 2001]. In the Northern Hemisphere, we have the North Atlantic (NA) region, following the definition of Khatiwala *et al.* [2012]. The region north of STF, as well as the rest of the world ocean, are defined as the OTHER region. The NA region covers the Labrador, Irminger, Nordic and Barent Seas, NADW forms. However, the NA region also covers some North Atlantic mode water formation regions in the mid-latitudes.

Figure 4.3 shows the water-mass fractions regardless of transit time ($\tau^* = 0$ in Equation 4.7), partitioned according to last ventilation region. Together, these different fractions account for all the water at any point in the interior ocean and hence they sum to unity. We see that Southern Ocean waters are a mixture of waters last ventilated in various regions of the world ocean, highlighting the importance of mixing in ocean transport. In the early 1990s, CDW is dominated by south-of-SB fraction (up to 70%). LCDW, the denser part of CDW, is where NADW can be found, containing a NA-ventilated fraction of up to 20% (50% in the Atlantic sector). AAIW is dominated by water last ventilated between SB and SAF (up to 70%). SAMW is mostly comprised of water last ventilated between SAF and STF, consistent with the findings of Hanawa and Talley [2001]. The SAF-STF fraction is largest close to its density

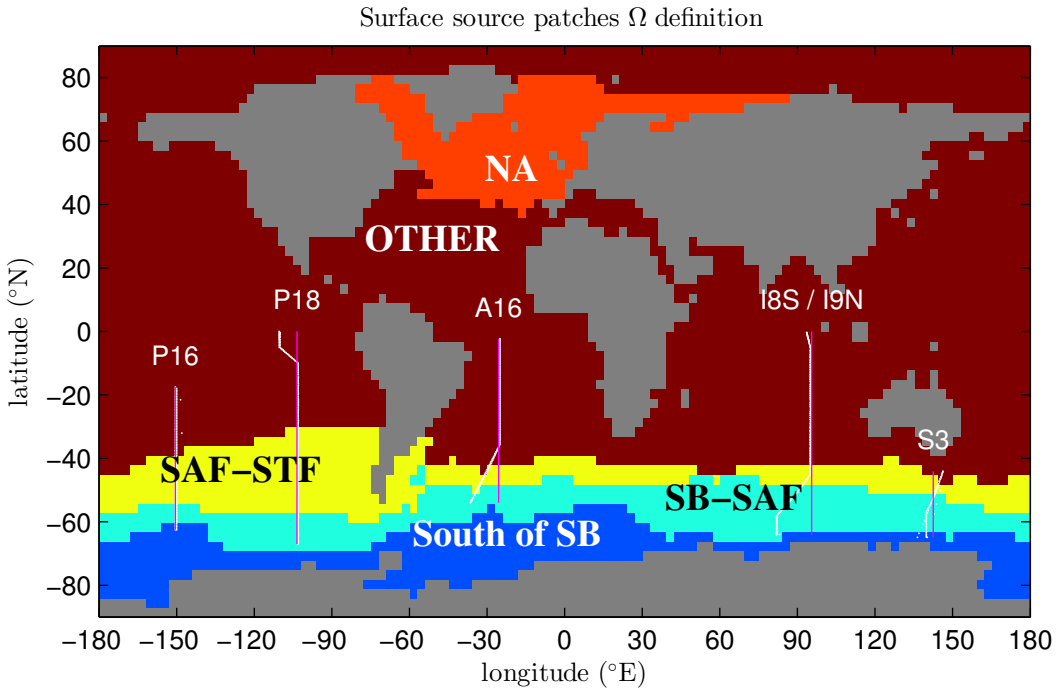


Figure 4.2: Surface regions Ω_i 's definition. Overlaid are magenta lines (white points) denoting the nominal (actual) positions of the hydrography samples.

outcrop (up to 60%), then decreases to below 30% in the tropics. The OTHER fraction is prominent in Atlantic and Indian SAMW (up to 80%). This may be due to northward fluctuations of the STF away from its climatological mean position *Orsi et al.* [1995] into OTHER region. STMW is dominated by the OTHER fraction, locally taking up \sim 50–100%. The Atlantic sector STMW also contains a moderate NA fraction (up to 20%).

We note that *McCartney* [1977] and *England et al.* [1993] suggest that the AAIW formation region is not circumpolar, but localized. Our circumpolar partition of the Southern Ocean surfaces prevents us from either supporting or contradicting these studies, but with a set of zonally partitioned surface region definition, or even to examine f as a function of surface locations \mathbf{r}_s rather than interior locations \mathbf{r} , the precise AAIW formation region can in principle be identified.

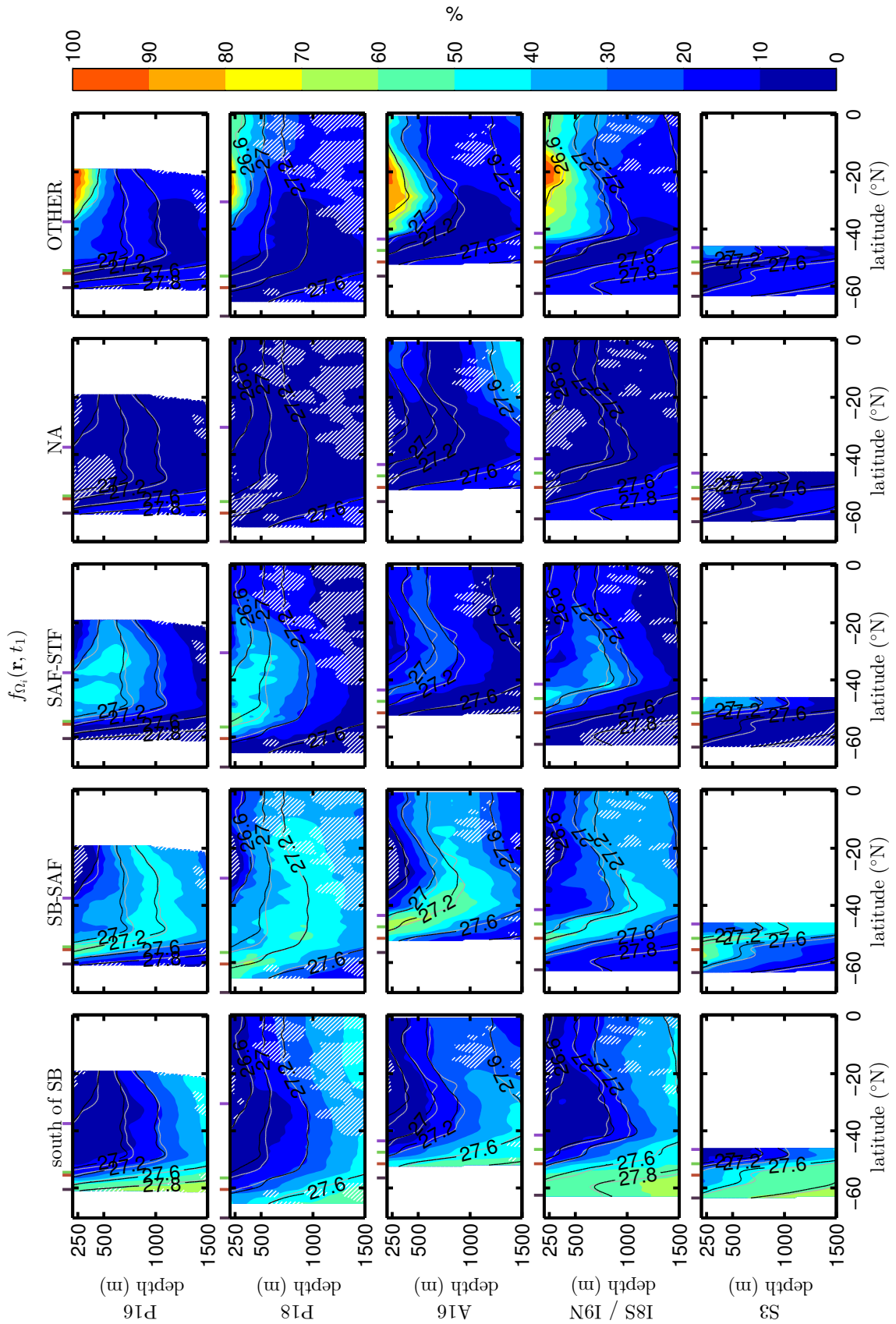


Figure 4.3: Water mass fraction of all transit time at t_1 , partitioned according to last ventilation location. Interior locations where the deconvolution does not converge, or where f_{n_i} is below 1%, are hatched in white. Potential density anomaly contours for t_1 and t_2 are shown in black and grey, respectively. See Figure 4.1 for potential density anomaly contours and ticks definitions.

Regional mean transit time, Γ_{Ω_i}

We also compute the mean transit time, Γ_{Ω_i} , for these fractions (called the regional mean transit time of water last ventilated from Ω_i), as shown in Figure 4.4. The regional mean transit times are obtained as the first τ -moment of the transit-time distribution conditional on last ventilation in Ω_i , that is,

$$\Gamma_{\Omega_i}(\mathbf{r}, t) \equiv \frac{\int_{\Omega_i} d^2 r_s \int_0^\infty d\tau \tau \mathcal{G}(\mathbf{r}, t; \mathbf{r}_s, \tau)}{\int_{\Omega_i} d^2 r_s \int_0^\infty d\tau \mathcal{G}(\mathbf{r}, t; \mathbf{r}_s, \tau)} \quad (4.8)$$

$$= \frac{\int_{\Omega_i} d^2 r_s \int_0^\infty d\tau \tau \mathcal{G}(\mathbf{r}, t; \mathbf{r}_s, \tau)}{f_{\Omega_i}(\mathbf{r}, t; 0)}. \quad (4.9)$$

Note that if the fraction $f_{\Omega_i}(\mathbf{r}, t; 0)$ is too small, the numerical computation runs into problems in the division and the resultant regional mean transit time is then uncertain.

The water-mass fractions last ventilated in the Southern Ocean fractions (i.e., in south-of-SB, SB-SAF, and SAF-STF) have similar regional mean age patterns $\Gamma_{\Omega_i}(\mathbf{r})$, with the south-of-SB fraction being the oldest and the SAF-STF fraction being the youngest. These SO fractions have a regional mean age of 200–400 yr within CDW south of 40°S. In the West Pacific and Indian Oceans, the SO fractions have a regional mean age of up to 1000 yr where they reach north of 20°S and become part of PDW and IDW, respectively. The SO fractions have a regional mean age of less than 200 yr within SAMW and STMW. The NA and OTHER fractions have similar features, because NA and OTHER share much of the North Atlantic mode-water formation regions. NA and OTHER fractions within LCDW are typically 400–600 yr old. In the higher latitudes just below the mixed layer, the NA and OTHER fractions are very small, rendering their regional mean transit time highly uncertain (division by small f_{Ω_i}). The NA and OTHER fractions within the PDW and IDW have regional mean transit time of 1200–1400, which is consistent with

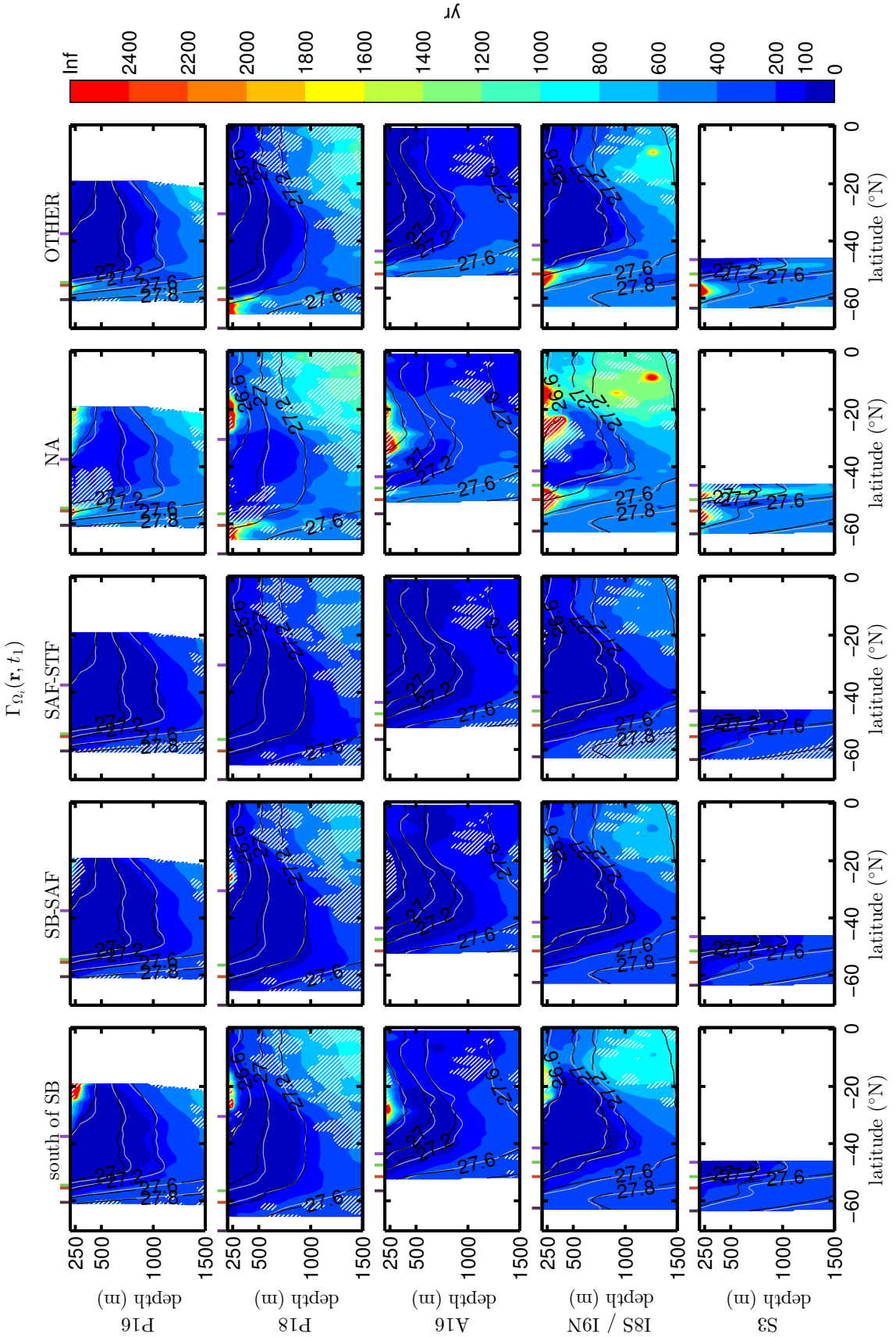


Figure 4.4: Regional mean transit time, at t_1 , of water according to its last ventilation regions. Interior locations where the deconvolution does not converge, or where f_{Ω_i} is below 1%, are hatched in white. Potential density anomaly contours for t_1 and t_2 are shown in black and grey, respectively. See Figure 4.2 for the ventilation region definitions and Figure 4.1 for potential density anomaly contours and ticks definitions.

their long transport path to the point of measurement. The tiny fractions of NA water within SAMW and STMW prevent their regional mean transit time being reliably estimated, while the OTHER fraction is typically younger than 200 yr in SAMW and STMW.

4.1.2 Decadal changes between early 1990s and mid-2000s

We now examine the changes in \mathcal{G} between the two observation times t_1 and t_2 , denoting changes in quantity X by δX . We note that the isopycnals have shifted between observations, and that the changes in any ventilation metric may be due to either changes on surfaces of constant density, or due to the movement of the isopycnals themselves, or both. [This was also noted by Waugh, 2014] To quantify the change on surfaces of constant density, we calculate the changes in σ_0 -latitude coordinates, and then, using the isopycnals at observation time t_1 , map the changes back to the depth-latitude space of t_1 . Subtracting the changes on surfaces of constant density from the total change then yields the changes due to the movements of the isopycnals. Figure C.1 in Appendix C shows the changes in density between the time of original and repeat hydrography. Because we see that changes in many diagnostics due to isopycnal movements merely reflect the density change pattern, and that filtering these changes out yields a set of more coherent and instructive signals, we choose to focus on changes occurring on surfaces of constant density mapped back to depth.

*Change in water-mass fraction older than τ^**

To identify the transit time threshold τ^* for which $\delta f(\mathbf{r}; \tau^*)$ is greatest, we examine the change in $f(\mathbf{r}, t; \tau^*)$ as a function of τ^* and latitude, volume-averaged from 250 to 1500m depth. To isolate changes in different water masses, we separately plot the changes volume-averaged over CDW ($\sigma_0 \geq 27.2 \text{ kg m}^{-3}$), and over SAMW and STMW ($\sigma_0 = 26.6\text{--}27.2 \text{ kg m}^{-3}$) in Figure 4.5a and 4.5b, respectively.

From Figure 4.5a, CDW shows a complex dependence of δf with respect to τ^* , with δf changing sign multiple times with increasing transit time threshold τ^* . The increase in f is at a maximum for $\tau^* \sim 60$ yr towards its outcrop south of 40°S , and for $\tau^* \sim 160$ yr away from its outcrop and towards north. The intermittent decrease in f is maximum for $\tau^* \sim 50$ yr. SAMW and STMW (Figure 4.5b) exhibit a comparatively more coherent increase of older water mass fraction south of 40°S and a decrease of older water mass fraction between 40°S and 20°S . The maximum of the changes occurs at τ^* being 10–50 yr.

We therefore focus on $\delta f(\mathbf{r}; 30 \text{ yr})$ in Figure 4.6a. There is a clear dipolar pattern of increased $f(\mathbf{r}; 30 \text{ yr})$ south of $\sim 40^\circ\text{S}$ and decreased $f(\mathbf{r}; 30 \text{ yr})$ north of $\sim 40^\circ\text{S}$. South of $\sim 40^\circ\text{S}$, the $\sim 20\%$ decade $^{-1}$ increase in the fraction of water older than 30 yr encompasses CDW and the southern tip of AAIW and SAMW. North of $\sim 40^\circ\text{S}$, the fraction of water older than 30 yr decreases by $\sim 10\%$ decade $^{-1}$ in SAMW and STMW. It is noted that 40°S is where the isopycnals cease their sharp descent and begin gradually ascending to the north.

It is possible that the dipolar water-mass fraction change seen in Figure 4.6a indicates a northward shift of Southern Ocean water masses. However, more analysis would have to be made to see if this is indeed the case. (E.g., postulating corresponding f_{Ω_i} change and examine if the predicted changes really have taken place.)

Changes in global mean transit time

Figure 4.6b shows the change in the global mean transit time as a percentage of its average over the two observation times, i.e., $\delta\Gamma(\mathbf{r})/\bar{\Gamma}(\mathbf{r})$, where $\bar{\Gamma}(\mathbf{r}) \equiv \frac{1}{2}(\Gamma(\mathbf{r}, t_2) + \Gamma(\mathbf{r}, t_1))$. Generally consistent with the dipolar $\delta f(\mathbf{r}; 30 \text{ yr})$ feature, mean transit time is on increase (decrease) by $\sim 80\%$ decade $^{-1}$ south (north) of $\sim 40^\circ\text{S}$. Within this dipolar mean transit time change, the increase is most intense in section P16, most widespread in section A16, and weakest in section P18. The Indian section is more noisy than the other sections but nevertheless has a similar pattern of $\delta\Gamma$ to other sections. A feature not found

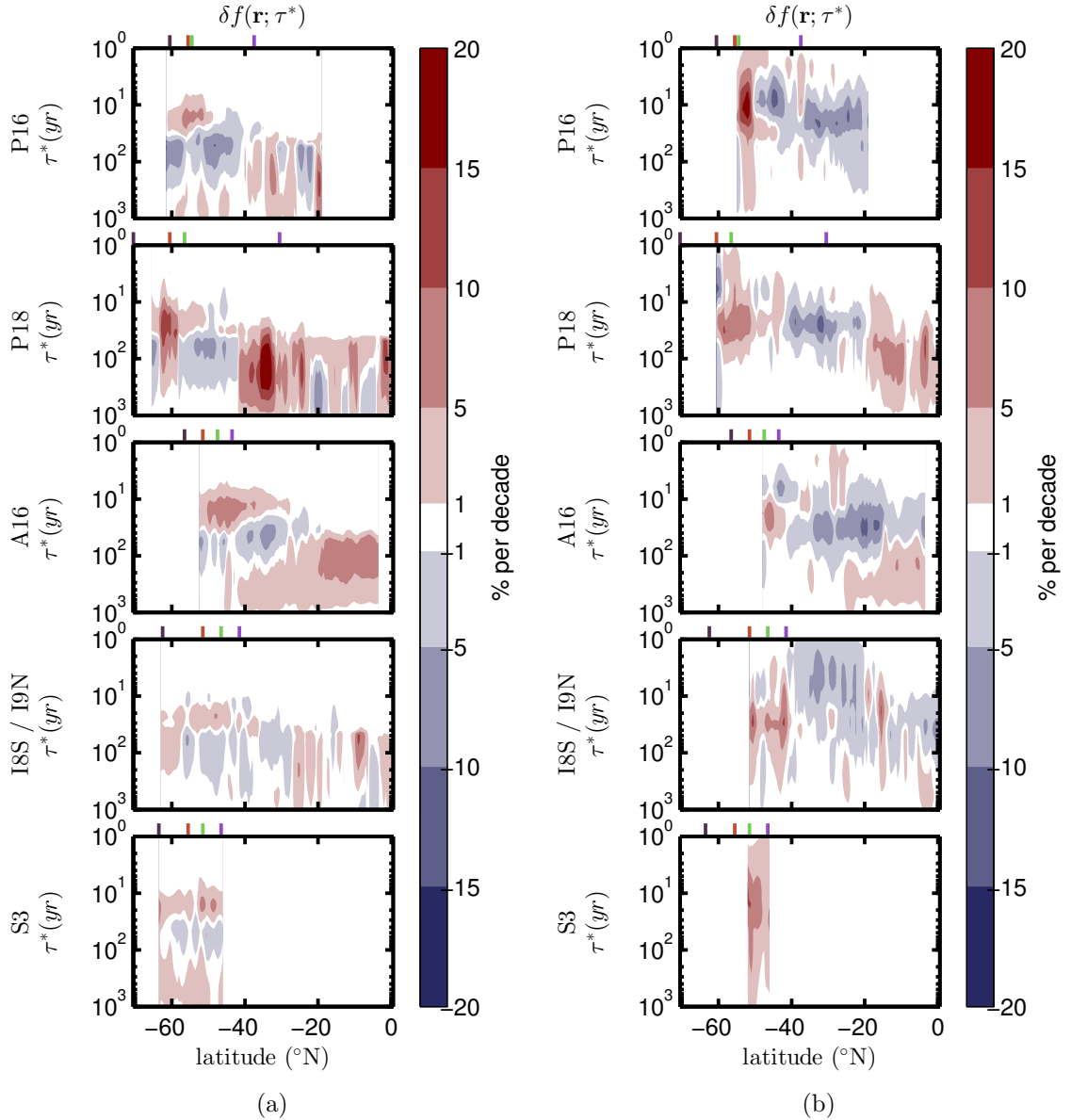


Figure 4.5: Change in water mass fractions classified by transit time. (a) Change in water mass fraction of transit time exceeding τ years, plotted as a function of τ for water volume-averaged from 250 m to 1500 m depth, below the 27.2 kg m^{-3} isopycnals. (b) Same as (a), but above the 27.2 kg m^{-3} isopycnals. See Figure 4.1 for ticks definitions.

in $\delta f(\mathbf{r}, 30 \text{ yr})$ is a decrease of mean transit time by 40–80% decade $^{-1}$ close to 60°S in the Pacific sector. This may be due to the enhanced upwelling of CDW driving faster AABW formation.

It is interesting to see that the sign of $\delta f(\mathbf{r}; 30 \text{ yr})$ does not always correspond to the sign of $\Gamma(\mathbf{r})$. Differences reflect the different information captured by these diagnostics: with the relatively short τ^* cutoff, the $\delta f(\mathbf{r}; \tau^*)$ highlights the changes at the shorter transit times, while the $\delta\Gamma(\mathbf{r})$ are more strongly affected by the TTD’s tail behaviour. The changes $\delta f(\mathbf{r}; 30 \text{ yr})$ and $\delta\Gamma(\mathbf{r})$ hence provide complementary information on the ventilation changes.

Changes in TTD width

We plot the percentage change of Δ/Γ in Figure 4.6c. In close proximity to PF, AAIW exhibits a decrease in Δ/Γ by $\sim 20\%$. The extent of decrease varies greatly between sections, with the smallest extent in P16 and greatest in P18 and I8S/I9N. For SAMW and STMW Δ/Γ has increased by $\sim 40\%$ decade $^{-1}$ in all sections. This suggests that mixing in the Southern Ocean has weakened within AAIW and strengthened within SAMW and STMW.

Changes in water-mass fractions last ventilated in Ω_i

We now focus on the changes in the ventilation location Ω_i , i.e., on the difference $\delta f_{\Omega_i}(\mathbf{r}; 0)$ plotted in Figure 4.7. Note that because the sum of these water-mass fractions accounts for 100% of the water an increase in the fraction ventilated in one region must always be accompanied by a decrease in fraction ventilated in regions, and that $\sum_i \delta f_{\Omega_i}(\mathbf{r}; 0) = 0$ for all interior location \mathbf{r} .

Within CDW and to the south of 40°S in general, we see NA-ventilated water fraction having increased by $\sim 3\%$ per decade, replacing south-of-SB ventilated water and the SB-SAF ventilated fraction. This is most prominent in the Atlantic sector where a $\sim 5\%$ per decade increase is also observed in the deep tropics, but is absent in Pacific section P18. Within SAMW, we see an increase in the SAF-STF fraction, replacing the NA-ventilated and OTHER fractions in all sections. Again, it is most prominent in the Atlantic sector with

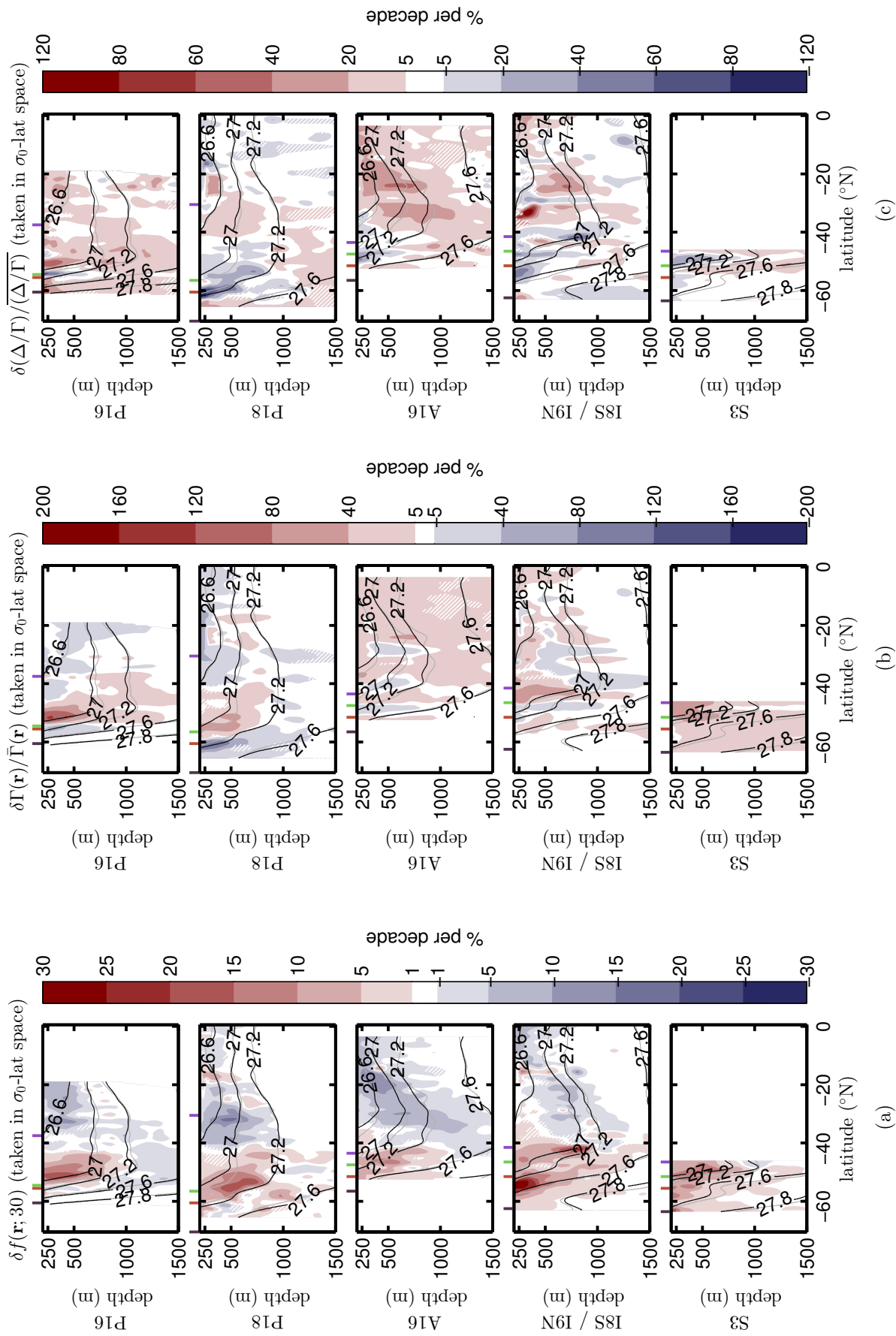


Figure 4.6: (a) Change in water mass fraction of transit time exceeding 30 years. (b) Change in the global mean age as percentage of average global mean age. (c) Change in the ratio Δ/Γ . For all plots, changes within one ensemble standard deviation, as well as locations where the deconvolution did not converge, are hatched in white. See Figure 4.1 for potential density anomaly contours and ticks definitions.

an up to $\sim 15\%$ per decade increase, while other sections exhibit on average a $\sim 7\%$ per decade increase. The increased Southern Ocean-ventilated fraction in SAMW and STMW is consistent with an increased northward Ekman drift. Enhanced Ekman suction may also have contributed to drawing up increased amount of NA-ventilated water into CDW.

Changes in regional mean transit time, $\delta\Gamma_{\Omega_i}$

Figure 4.8 shows the regional mean-transit-time changes as a percentage of their t_1, t_2 average, i.e., we plotted $\delta\Gamma_{\Omega_i}(\mathbf{r}) / \bar{\Gamma}_{\Omega_i}(\mathbf{r})$ for different surface region Ω_i , where $\bar{\Gamma}_{\Omega_i}(\mathbf{r}) \equiv \frac{1}{2}(\Gamma_{\Omega_i}(\mathbf{r}, t_2) + \Gamma_{\Omega_i}(\mathbf{r}, t_1))$.

Generally, changes in mean age are found to be similar among water-masses last ventilated in different regions. The south-of-SB fraction has a relatively higher percentage increase in mean age in water south of 40°S , with P16 showing the greatest increase ($\sim 120\text{--}150\%$ per decade), while the SAF-STF fraction has a relatively higher percentage decrease ($\sim -120\text{--}150\%$ per decade) within the lighter part of AAIW ($\sigma_0 = 27.2\text{--}27.6 \text{ kg m}^{-3}$). Close to 60°S in the Pacific sector, the regional mean ages of the south-of-SB, SB-SAF and SAF-STF fractions (i.e., all fractions last ventilated in the Southern Ocean) have decreased all by at least 30%.

With stronger upwelling due to the poleward-strengthening westerly winds, one might expect a reduction in the mean transit time of water from the NA surface to CDW in the Southern Ocean. However, such a mean transit time reduction is not seen except perhaps in P18. It should be noted that on its path from the North Atlantic surface to the Southern Ocean, the water is subject to transport changes not just within the Southern Ocean, but also in the North and South Atlantic. The mean age change estimated here is the net integrated effect of transport halfway around the globe and should not be expected to be controlled solely by processes in the Southern Ocean. The high degree of similarity between $\delta\Gamma_{\Omega_i}$ for water ventilated in the Ω_i regions may be due to the diffusive transport rendering the water parcels ‘losing memory’ of

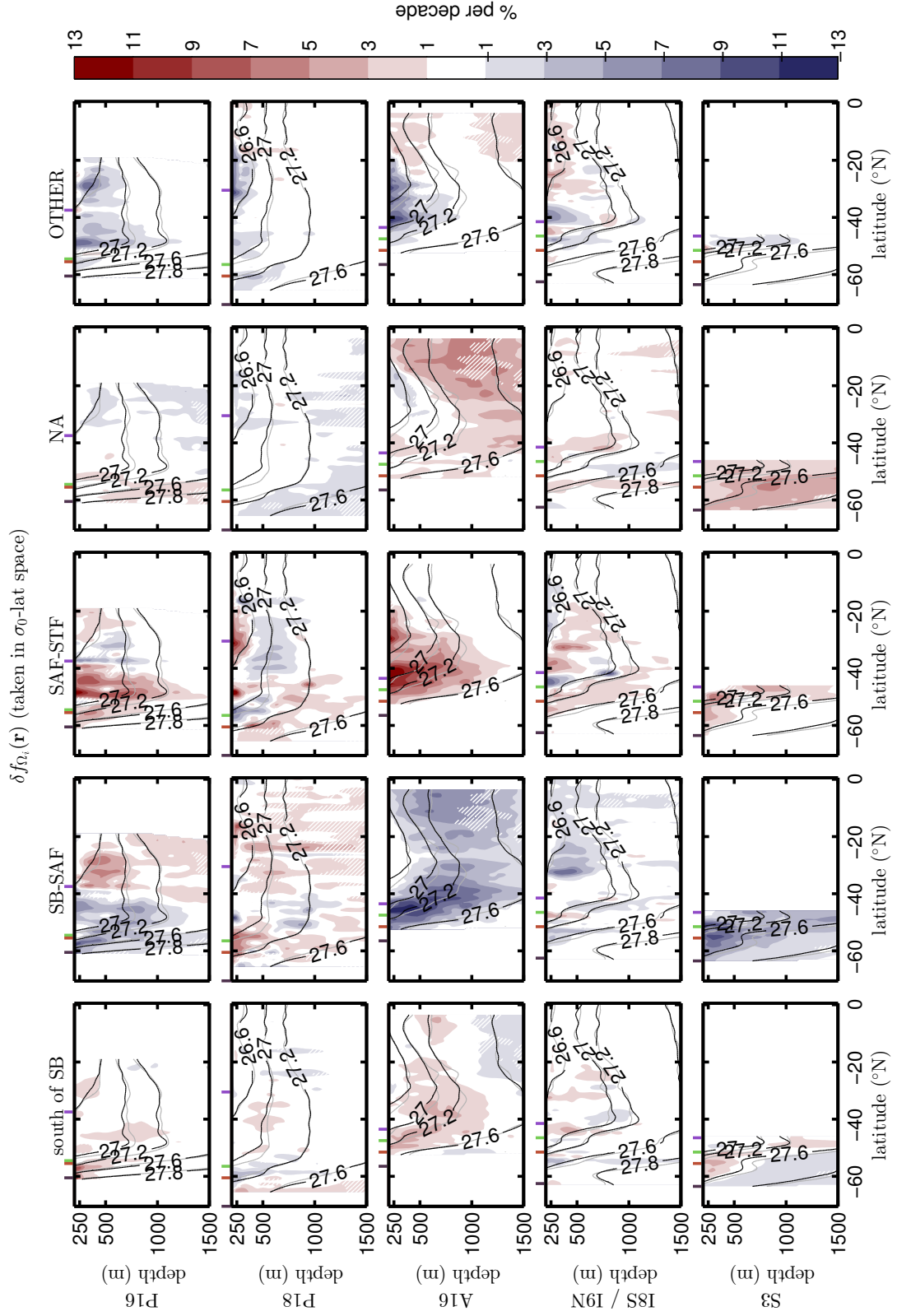


Figure 4.7: Changes within one ensemble standard deviation, as well as locations where the deconvolution did not converge, are hatched in white. See Figure 4.1 for potential density anomaly contours and ticks definitions.

its surface origin. It may also be that the information in the tracers used does not warrant robust inferences on the Ω -specific changes. There is too little NA fraction (below 1%) within most part SAMW and STMW for its Γ_{Ω_i} change to be reliably estimated.

Regional decomposition of global mean transit time changes

The global mean transit time $\Gamma(\mathbf{r}, t)$ can change due to changes in how much of the water at (\mathbf{r}, t) was last ventilated in different parts of the ocean, due to changes in the transit times from a given ventilation region, or due to both these factors combined. The boundary-propagator framework allows us to quantify how much these different processes contribute to $\delta\Gamma(\mathbf{r})$.

To this end, note that Γ can be formulated as a linear combination of regional mean transit times with the water-mass fractions f_{Ω_i} as weights (for brevity, we suppress the τ^* argument in $f_{\Omega_i}(\mathbf{r}, t; \tau^*)$ when $\tau^* = 0$, i.e., regardless of transit time):

$$\Gamma(\mathbf{r}, t) = \sum_i f_{\Omega_i}(\mathbf{r}, t) \Gamma_{\Omega_i}(\mathbf{r}, t) \quad (4.10)$$

where the sum is over all patches Ω_i tiling the global ocean surface. If we write $f_{\Omega_i}(\mathbf{r}, t_2) = f_{\Omega_i}(\mathbf{r}, t_1) + \delta f_{\Omega_i}(\mathbf{r})$ and $\Gamma_{\Omega_i}(\mathbf{r}, t_2) = \Gamma_{\Omega_i}(\mathbf{r}, t_1) + \delta\Gamma_{\Omega_i}(\mathbf{r})$, then we have

$$\begin{aligned} \Gamma(\mathbf{r}, t_2) &= \sum_i f_{\Omega_i}(\mathbf{r}, t_2) \cdot \Gamma_{\Omega_i}(\mathbf{r}, t_2) \\ &= \sum_i [f_{\Omega_i}(\mathbf{r}, t_1) + \delta f_{\Omega_i}(\mathbf{r})] [\Gamma_{\Omega_i}(\mathbf{r}, t_1) + \delta\Gamma_{\Omega_i}(\mathbf{r})] \\ &= \Gamma(\mathbf{r}, t_1) + \sum_i f_{\Omega_i}(\mathbf{r}, t_1) \delta\Gamma_{\Omega_i}(\mathbf{r}) \\ &\quad + \sum_i \Gamma_{\Omega_i}(\mathbf{r}, t_1) \delta f_{\Omega_i}(\mathbf{r}) + \sum_i \delta f_{\Omega_i}(\mathbf{r}) \delta\Gamma_{\Omega_i}(\mathbf{r}). \end{aligned} \quad (4.11)$$

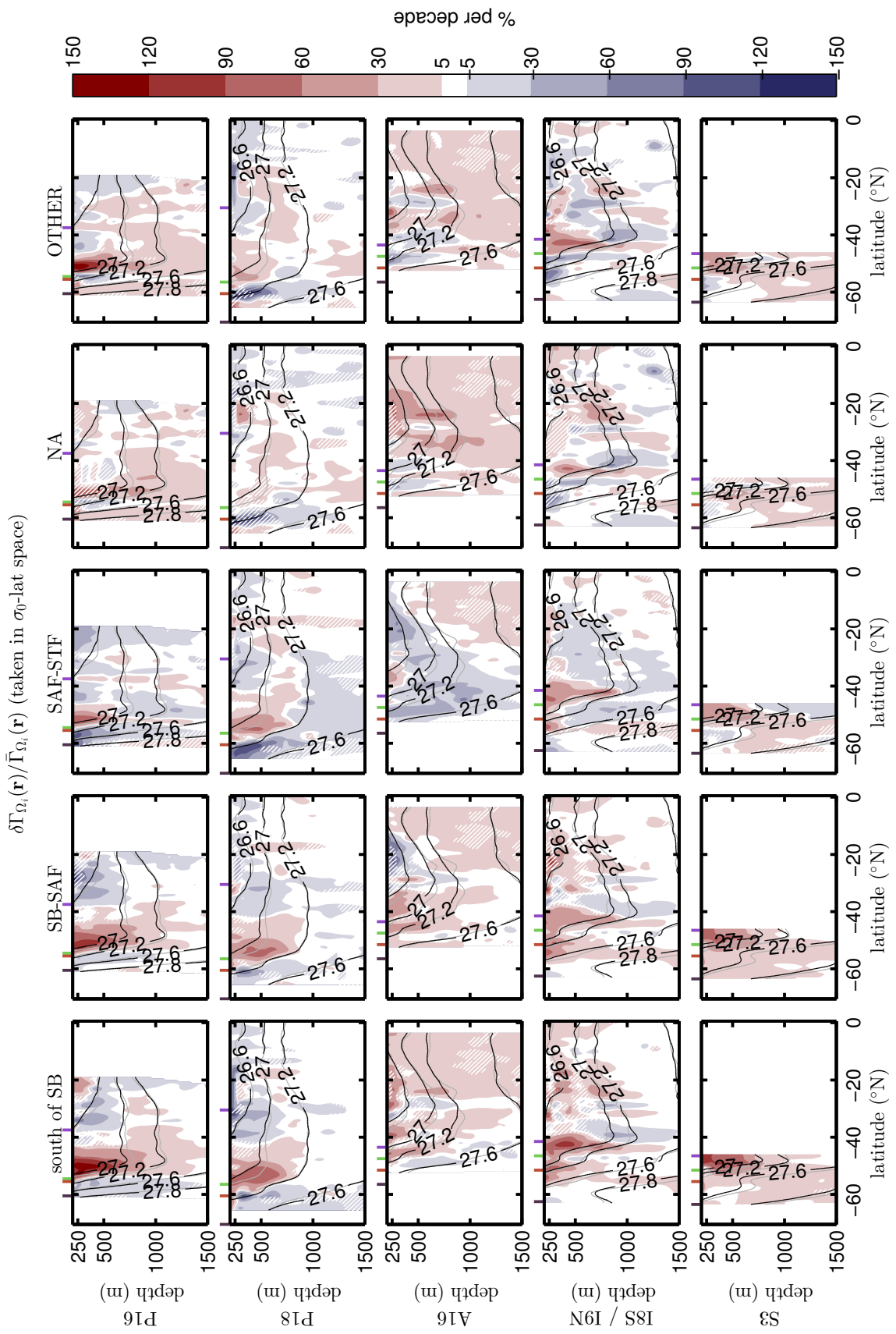


Figure 4.8: Changes of regional mean age as percentages of their respective average regional mean age. Changes within ensemble standard deviation, as well as locations where f_{Ω_i} falls below 1% or the deconvolution did not converge, are hatched in white. See Figure 4.1 for potential density anomaly contours and ticks definitions.

Thus, the change in global mean transit time is given by

$$\begin{aligned}
\delta\Gamma(\mathbf{r}) &= \sum_i \Gamma_{\Omega_i}(\mathbf{r}, t_1) \delta f_{\Omega_i}(\mathbf{r}) + \sum_i f_{\Omega_i}(\mathbf{r}, t_1) \delta\Gamma_{\Omega_i}(\mathbf{r}) + \sum_i \delta f_{\Omega_i}(\mathbf{r}) \delta\Gamma_{\Omega_i}(\mathbf{r}) \\
&= \left(\begin{array}{c} \text{change due to} \\ \text{change in fraction composition} \end{array} \right) \\
&\quad + \left(\begin{array}{c} \text{change due to} \\ \text{change in regional mean transit times} \end{array} \right) \\
&\quad + \left(\begin{array}{c} \text{cross} \\ \text{terms} \end{array} \right). \tag{4.12}
\end{aligned}$$

The changes due to δf_Ω (term 1), due to $\delta\Gamma_\Omega$ (term 2), and due to the interaction of the two (term 3), are presented in Figure 4.9, 4.10 and 4.11, respectively. The changes are plotted as percentages of $\bar{\Gamma}_\Omega$, so the three figures sum up to that of $\delta\Gamma/\bar{\Gamma}$ as in Figure 4.6b.

The inferred mean age change of CDW comes predominantly from the interplay of $\delta\Gamma_{SO}$ (that is, $\delta\Gamma_{sSB} + \delta\Gamma_{SB-SAF} + \delta\Gamma_{SAF-STF}$) and δf_{NA} . For instance, the increase in global mean transit time into CDW is due to increased $\delta\Gamma_{SO}$ and increased δf_{NA} which has typically long transit time. Thus SO-ventilated water is getting both older itself, while being diluted with yet older water from the NA. Conversely, decrease in global mean transit time into SAMW and STMW is due to decreased $\delta\Gamma_{SO}$ and decreased δf_{NA} . This means that the formation rate of SAMW is greater and carries less NA-ventilated water of very long transit time. Finally, the decrease in global mean transit time in the Pacific sector around 60°S is also due to decreased $\delta\Gamma_{SO}$. This is further amplified in Section P18 by decreased δf_{NA} , but is attenuated in Section P16 by increased δf_{NA} .

The OTHER fraction is also found to have large effect on the global mean transit time change. The decreased global mean transit time into the South Pacific at around 60°S is also due to the decrease of both $\delta\Gamma_{OTHER}$ and δf_{OTHER} , meaning that OTHER-ventilated water is exhibiting faster transport

into South Pacific CDW, but in smaller fractions. The widespread increase of global mean transit time into South Atlantic SAMW is also due to increased Γ_{OTHER} .

At some locations, our composition analysis is complicated by the presence of large cross terms due to both δf_{Ω_i} and $\delta \Gamma_{\Omega_i}$ having magnitudes similar to their base values. Upon closer examination, we see that $\delta f_{\Omega_i} \delta \Gamma_{\Omega_i}$ tends to be large when corresponding f_{Ω_i} are small (< 5%), making calculation of the Ω_i -ventilated water contribution highly uncertain. For all other locations the cross terms are less than 10% and changes in global mean transit time are captured by the primary terms.

4.2 Application: C_{ANT} storage rate in the Southern Ocean

One of the key uses of the boundary propagator is the calculation of the interior concentration of a tracer of interest via a simple convolution with the geographically distributed surface history. Given a ME-estimated boundary propagator $\mathcal{G}(\mathbf{r}, t_a; \mathbf{r}_s, \tau)$ for interior location \mathbf{r} at deconvolution time t_a and the surface history of a tracer $C^S(\mathbf{r}_s, t)$ for all surface source locations \mathbf{r}_s and for t ranging from far back into the past to t_a , we can estimate the tracer concentration C^I at time t_a and interior location \mathbf{r} as

$$\hat{C}^I(\mathbf{r}, t_a) = \int d^2 r_s \int_0^\infty d\tau \mathcal{G}(\mathbf{r}, t_a; \mathbf{r}_s, \tau) C^S(\mathbf{r}_s, t_a - \tau). \quad (4.13)$$

Generally, a \mathcal{G} estimated by deconvolved at time t_a can only be used to propagate the surface history to provide \hat{C}^I at t_a . However, if we additionally assume steady transport such that \mathcal{G} at another time t_b is the same as at t_a , then we can compute \hat{C}^I at t_b by applying (4.13), but substituting $\mathcal{G}(\mathbf{r}, t_a; \mathbf{r}_s, \tau)$

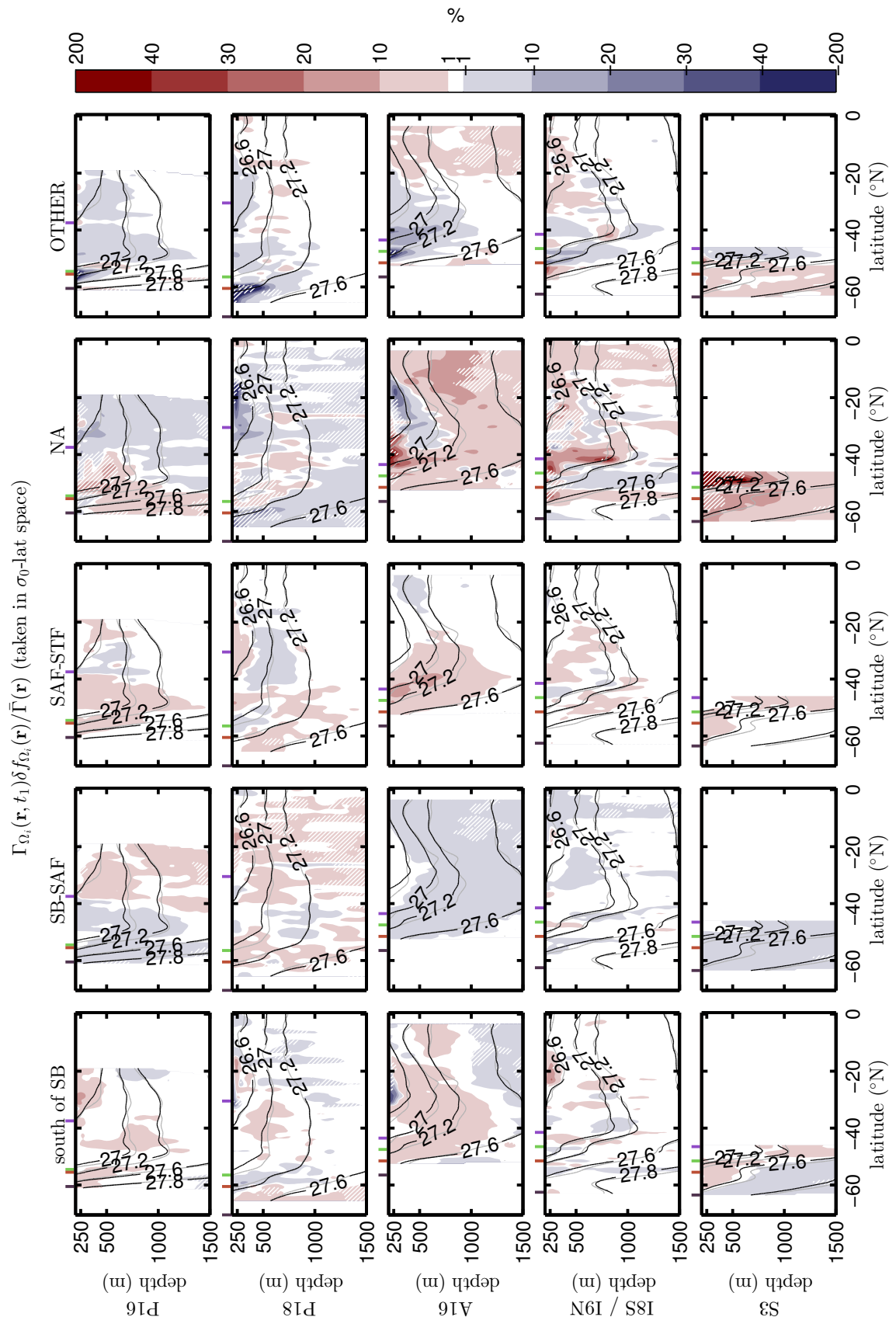


Figure 4.9: Percentage of $\delta\Gamma/\bar{\Gamma}$ due to fraction composition changes. Changes within ensemble standard deviation, as well as locations where f_{Ω_i} falls below 1% or the deconvolution did not converge, are hatched in white. See Figure 4.1 for potential density anomaly contours and ticks definitions.

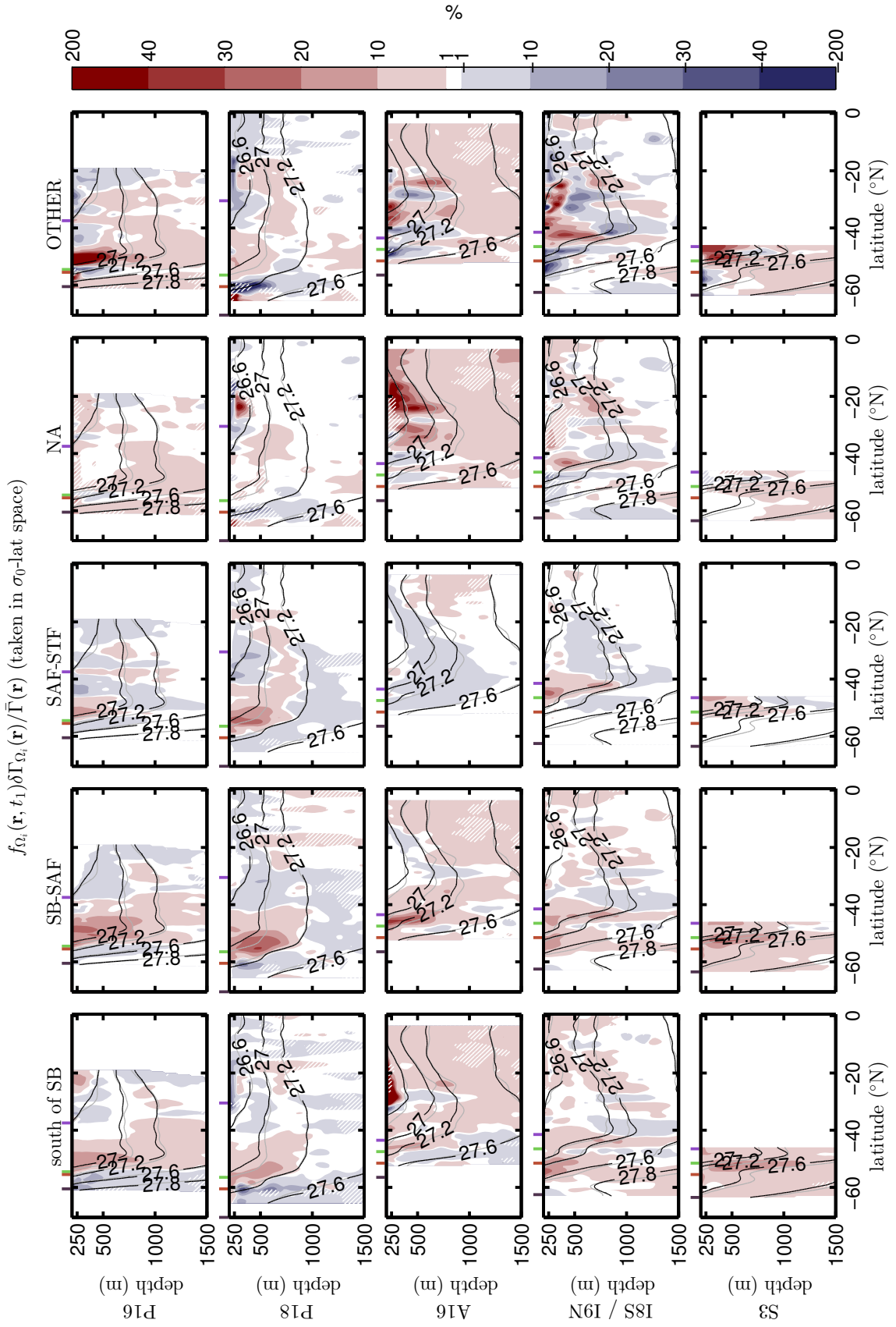


Figure 4.10: Percentage of $\delta\Gamma/\bar{\Gamma}$ due to regional mean age changes. Changes within ensemble standard deviation, as well as locations where f_{Ω_i} falls below 1% or the deconvolution did not converge, are hatched in white. See Figure 4.1 for potential density anomaly contours and ticks definitions.

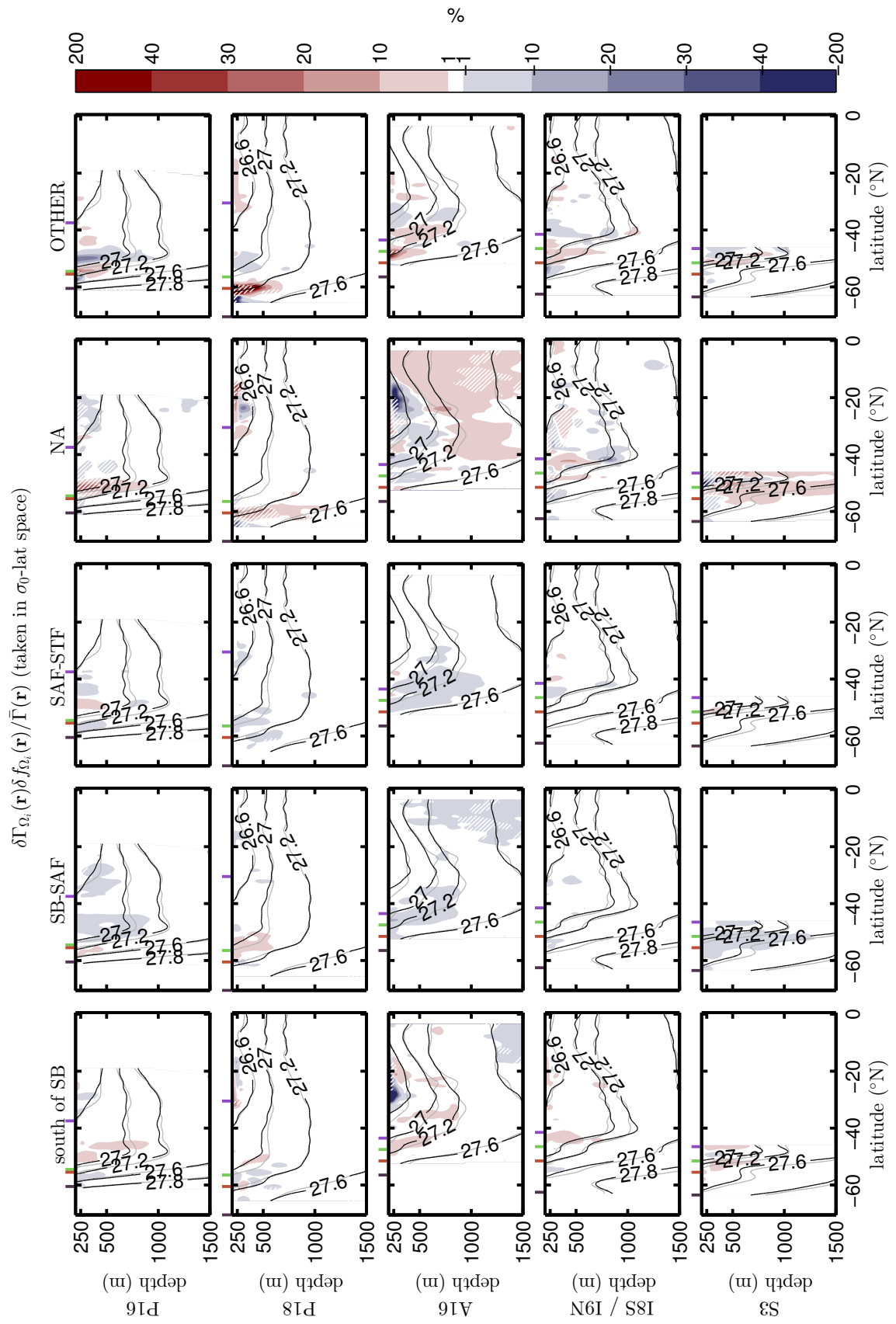


Figure 4.11: Percentage of $\delta\Gamma/\bar{\Gamma}$ due to compound effects of δf_{Ω_i} and $\delta\Gamma_{\Omega_i}$. Changes within ensemble standard deviation, as well as locations where f_{Ω_i} falls below 1% or the deconvolution did not converge, are hatched in white. See Figure 4.1 for potential density anomaly contours and ticks definitions.

for $\mathcal{G}(\mathbf{r}, t_b; \mathbf{r}_s, \tau)$, to obtain

$$\int d^2 r_s \int_0^\infty d\tau \mathcal{G}(\mathbf{r}, t_a; \mathbf{r}_s, \tau) C^S(\mathbf{r}_s, t_b - \tau) \equiv \hat{C}^I(\mathbf{r}, t_b; \mathcal{G}_{t_a}), \quad (4.14)$$

where an extra parameter is specified for \hat{C}^I to indicate the use of \mathcal{G} that has a different deconvolution time (Note that the surface history C^S is still used up to t_b). The ability to compute the interior tracer concentration at the deconvolution time, as well as any other time assuming steady transport, will be exploited as follows.

For tracers with known surface history but interior concentration that is difficult or impossible to measure, we can use the inferred boundary propagator to estimate their interior concentration as a function time using (4.13). For example, C_{ANT} cannot be measured but must be inferred in this way. *Waugh et al.* [2013], using a TTD method on CFC-12 measurements, infer decadal changes in Southern Ocean transport. However, the TTD's are only simple approximations to \mathcal{G} . Here, we use less limited estimates of \mathcal{G} itself (not just the global TTD) to infer the concentration of C_{ANT} and to separate these changes into those due to the changing atmospheric CO₂ concentration and those due to changing transport.

At time t_2 , C^I is given by the convolution

$$C^I(\mathbf{r}, t_2) = \int d^2 r_s \int_0^\infty d\tau \mathcal{G}(\mathbf{r}, t_2; \mathbf{r}_s, \tau) C^S(\mathbf{r}_s, t_2 - \tau). \quad (4.15)$$

Now the interior concentration of a conserved tracer can change due to rising/declining surface concentration (i.e., C^S), or due to a change in the

oceanic surface-to-interior transport (\mathcal{G}). We define the changes in \mathcal{G} as

$$\delta\mathcal{G}(\mathbf{r}; \mathbf{r}_s, \tau) \equiv \mathcal{G}(\mathbf{r}, t_2; \mathbf{r}_s, \tau) - \mathcal{G}(\mathbf{r}, t_1; \mathbf{r}_s, \tau) \quad (4.16)$$

and the changes in surface tracer history as

$$\delta C^S(\mathbf{r}_s, \tau) \equiv C^S(\mathbf{r}_s; t_2 - \tau) - C^S(\mathbf{r}_s; t_1 - \tau). \quad (4.17)$$

Note that the difference for both quantities is computed at corresponding transit times τ . For example, $\mathcal{G}(\mathbf{r}, t_1; \mathbf{r}_s, \tau)$ and $\mathcal{G}(\mathbf{r}, t_2; \mathbf{r}_s, \tau)$ are shifted to a common observation time before taking the difference at the same τ . It then follows that

$$\begin{aligned} \mathcal{G}(\mathbf{r}, t_2; \mathbf{r}_s, \tau) C^S(\mathbf{r}_s; t_2 - \tau) &= \mathcal{G}(\mathbf{r}, t_1; \mathbf{r}_s, \tau) C^S(\mathbf{r}_s; t_2 - \tau) \\ &\quad + \delta\mathcal{G}(\mathbf{r}; \mathbf{r}_s, \tau) C^S(\mathbf{r}_s; t_2 - \tau) \\ &= \mathcal{G}(\mathbf{r}, t_1; \mathbf{r}_s, \tau) C^S(\mathbf{r}_s; t_1 - \tau) \\ &\quad + \mathcal{G}(\mathbf{r}, t_1; \mathbf{r}_s, \tau) \delta C^S(\mathbf{r}_s; \tau) \\ &\quad + \delta\mathcal{G}(\mathbf{r}; \mathbf{r}_s, \tau) C^S(\mathbf{r}_s; t_2 - \tau) \end{aligned} \quad (4.18)$$

(Note that the surface concentration of the last term is left intentionally in terms of $t_2 - \tau$; hence there is no $\delta\mathcal{G}\delta C^S$ term.) Integrating both sides across

all ventilation region and transit time propagates the surface histories to give

$$\begin{aligned}
C^I(\mathbf{r}, t_2) &= C^I(\mathbf{r}, t_1) \\
&+ \int d^2 r_s \int_0^\infty d\tau \mathcal{G}(\mathbf{r}, t_1; \mathbf{r}_s, \tau) \delta C^S(\mathbf{r}_s, \tau) . \\
&+ \int d^2 r_s \int_0^\infty d\tau \delta \mathcal{G}(\mathbf{r}; \mathbf{r}_s, \tau) C^S(\mathbf{r}_s, t_2 - \tau) \quad (4.19)
\end{aligned}$$

Hence

$$\begin{aligned}
\delta C^I(\mathbf{r}) \equiv C^I(\mathbf{r}, t_2) - C^I(\mathbf{r}, t_1) &= \int d^2 r_s \int_0^\infty d\tau \mathcal{G}(\mathbf{r}, t_1; \mathbf{r}_s, \tau) \delta C^S(\mathbf{r}_s, \tau) \\
&+ \int d^2 r_s \int_0^\infty d\tau \delta \mathcal{G}(\mathbf{r}; \mathbf{r}_s, \tau) C^S(\mathbf{r}_s, t_2 - \tau) . \quad (4.20)
\end{aligned}$$

The term on the left of Equation 4.20 is the total interior concentration change. The first term on the right is the change that is solely due to the changes in the surface history, in absence of any circulation change, examined at t_2 . The second term on the right is the change that is due to a new circulation, given the surface history from t_2 back in time. These three terms can be readily calculate from our ME-estimated \mathcal{G} 's given the C_{ANT} surface history.

From equations 4.16, 4.17 and 4.14, we have

$$\begin{aligned}
\int d^2 r_s \int_0^\infty d\tau \mathcal{G}(\mathbf{r}, t_1; \mathbf{r}_s, \tau) \delta C^S(\mathbf{r}_s, \tau) &= \int d^2 r_s \int_0^\infty d\tau \mathcal{G}(\mathbf{r}, t_1; \mathbf{r}_s, \tau) C^S(\mathbf{r}_s; t_2 - \tau) \\
&- \int d^2 r_s \int_0^\infty d\tau \mathcal{G}(\mathbf{r}, t_1; \mathbf{r}_s, \tau) C^S(\mathbf{r}_s; t_1 - \tau) \\
&\approx \hat{C}^I(\mathbf{r}, t_2; \mathcal{G}_{t_1}) - \hat{C}^I(\mathbf{r}, t_1) \quad (4.21)
\end{aligned}$$

and

$$\begin{aligned}
\int d^2 r_s \int_0^\infty d\tau \delta \mathcal{G}(\mathbf{r}; \mathbf{r}_s, \tau) C^S(\mathbf{r}_s, t_2 - \tau) &= \int d^2 r_s \int_0^\infty d\tau \mathcal{G}(\mathbf{r}, t_2; \mathbf{r}_s, \tau) C^S(\mathbf{r}_s, t_2 - \tau) \\
&\quad - \int d^2 r_s \int_0^\infty d\tau \mathcal{G}(\mathbf{r}, t_1; \mathbf{r}_s, \tau) C^S(\mathbf{r}_s, t_2 - \tau) \\
&\approx \hat{C}^I(\mathbf{r}, t_2) - \hat{C}^I(\mathbf{r}, t_2; \mathcal{G}_{t_1}), \quad (4.22)
\end{aligned}$$

while the total difference $\delta C^I(\mathbf{r})$ is simply given by $\hat{C}^I(\mathbf{r}, t_2) - \hat{C}^I(\mathbf{r}, t_1)$.

To quantify the importance of the inferred changes in ocean transport for the global climate system, we now estimate the changes in Southern Ocean C_{ANT} concentrations that are purely due to changes in transport. We therefore compute all three terms of (4.20) for the tracer C_{ANT} and plot them in Figure 4.12. For ease of comparison with other studies, these are full changes computed in latitude-depth coordinates and not in σ_0 -depth coordinates.

We first examine the total decadal change in C_{ANT} in Figure 4.12a. The maximum increase in $C_{\text{ANT}} \sim 13 \mu\text{mol kg}^{-1}\text{decade}^{-1}$, which occurs in SAMW across all sections (except S3 which does not encompass mode waters). On examining greater depths (not shown), the increase can be seen to extend to as deep as 4500 m, tapering off to $\sim 1 \mu\text{mol kg}^{-1}\text{decade}^{-1}$. The 27.8 kg m^{-3} isopycnal, on which the tongue of LCDW lies, marks the C_{ANT} change minimum ($\sim 0 \mu\text{mol kg}^{-1}\text{decade}^{-1}$) with a C_{ANT} increase in less dense water masses above and with a C_{ANT} decrease in denser water below (including AABW). A slight decrease in C_{ANT} is inferred for IDW.

We next examine the attribution of changes in C_{ANT} to changes in C^S and \mathcal{G} in Figure 4.12b and 4.12c. As expected the total inferred δC_{ANT} is made up of a general increase everywhere due to the rising atmospheric CO₂ levels. However, there is also a change in ventilation, i.e., due to $\delta \mathcal{G}$. The general C_{ANT} change due to the rising atmospheric CO₂ has a maximum of $\sim 9 \mu\text{mol kg}^{-1}\text{decade}^{-1}$ close to the outcrops of SAMW and STMW, while the

changed transport results in $\sim 5 \mu\text{mol kg}^{-1}\text{decade}^{-1}$ decrease south of 40°S and $\sim 5 \mu\text{mol kg}^{-1}\text{decade}^{-1}$ increase in SAMW and STMW north of 40°S . On examining greater depth, the C_{ANT} decrease in AABW is predominantly due to the changed transport.

To quantify the spatially averaged, column-integrated change in C_{ANT} storage, we vertically integrate C_{ANT} over the 250–4500m water column and average with respect to latitude along each given section. To account for the fact that the measurements at high latitudes are representative of a smaller latitude circle, we weight latitude ϕ by $\sin \phi$. This is equivalent to computing an area average of the column integral over a one-degree longitude strip centred on the hydrography line. To account for the fact that 40°S divides the transport changes into two different regimes, we compute the average storage change separately north and south of 40°S . Table 4.2 collects the results in units of $\text{mol m}^{-2}\text{yr}^{-1}$.

We first compare, within each latitude band, the C_{ANT} storage change due to changes in \mathcal{G} with the total storage rate, as changes in \mathcal{G} affect these two latitude regions differently. Within the $40\text{--}60^\circ\text{S}$ band, changes in \mathcal{G} , which are likely due to enhanced upwelling of CDW, have varied effect on C_{ANT} storage, from $-0.1 \pm 0.05 \text{ mol m}^{-2} \text{ yr}^{-1}$ in the Indian Ocean section, to $0.22 \pm 0.05 \text{ mol m}^{-2} \text{ yr}^{-1}$ in Section P16. The changes in C_{ANT} mass-averaged across the five sections give zero significant overall C_{ANT} change. Within the $20\text{--}40^\circ\text{S}$ band, changes in \mathcal{G} , likely due to enhanced SAMW formation, result in an C_{ANT} increase in all sections, with Section P16 showing the strongest increase at $0.21 \pm 0.01 \text{ mol m}^{-2} \text{ yr}^{-1}$. Mass-averaging over all five sections, an average C_{ANT} increase of $0.116 \pm 0.006 \text{ mol m}^{-2} \text{ yr}^{-1}$ is inferred, which is about $\sim 21\%$ of the total C_{ANT} decadal change within the $20\text{--}40^\circ\text{S}$ band.

We then examine the change across the whole latitude band from 60°S to 20°S . Across the five sections, we obtain an average storage increase of $0.56 \pm 0.02 \text{ mol m}^{-2} \text{ yr}^{-1}$. We see that changes in \mathcal{G} act to reduce the C_{ANT} storage by

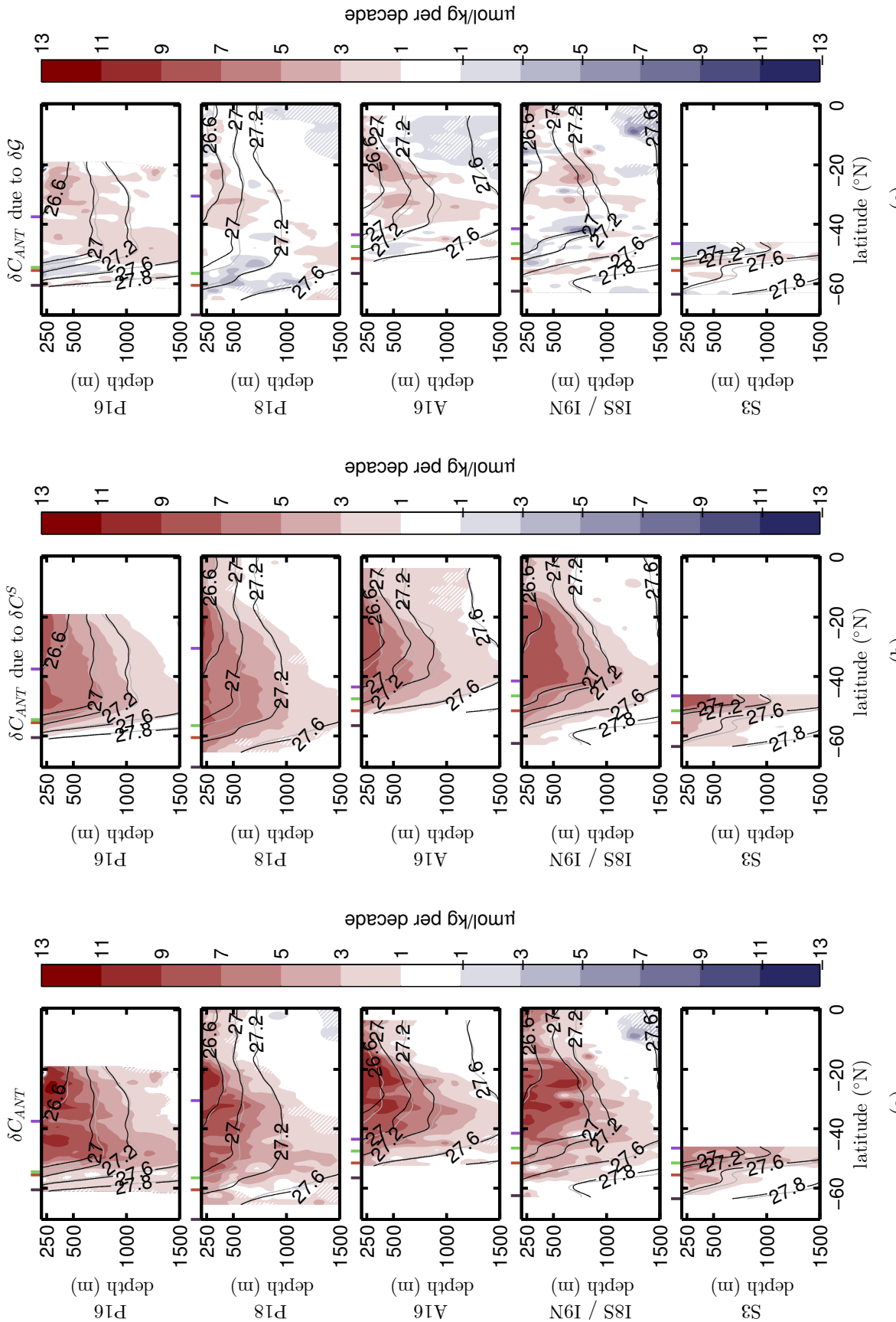


Figure 4.12: Inferred change in CANT classified as follows: (a) Total change (b) Change due to change in transport. (c) Change due to change in surface history (c) Change due to change in transport. Changes within ensemble standard deviation, as well as locations where f_{Ω_i} falls below 1% or the deconvolution did not converge, are hatched in white. See Figure 4.1 for potential density anomaly contours and ticks definitions.

Section	$60^{\circ}\text{S} \leq \phi < 40^{\circ}\text{S}$	$40^{\circ}\text{S} \leq \phi \leq 20^{\circ}\text{S}$	$60^{\circ}\text{S} \leq \phi \leq 20^{\circ}\text{S}$
Total C_{ANT} storage change ($\text{mol m}^{-2} \text{ yr}^{-1}$)			
P16	0.76 ± 0.06	0.63 ± 0.06	0.69 ± 0.06
P18	0.602 ± 0.007	0.412 ± 0.008	0.492 ± 0.006
A16	0.50 ± 0.02	0.627 ± 0.009	0.59 ± 0.01
I8S/I9N	0.46 ± 0.03	0.58 ± 0.02	0.532 ± 0.005
S3	0.38 ± 0.02	-	0.38 ± 0.02
average	0.56 ± 0.02	0.56 ± 0.02	0.56 ± 0.02
C_{ANT} storage change due to change in \mathcal{G} ($\text{mol m}^{-2} \text{ yr}^{-1}$)			
P16	0.22 ± 0.05	0.21 ± 0.01	0.21 ± 0.02
P18	0.03 ± 0.02	0.062 ± 0.006	0.05 ± 0.01
A16	0.1 ± 0.04	0.15 ± 0.01	0.13 ± 0.02
I8S/I9N	-0.1 ± 0.05	0.044 ± 0.007	-0.03 ± 0.02
S3	-0.03 ± 0.04	-	-0.03 ± 0.04
average	0.04 ± 0.04	0.116 ± 0.006	0.08 ± 0.02

Table 4.2: C_{ANT} storage change integrated over depth 250–4500m, one degree longitude and latitude bands (ϕ) for the hydrography sections indicated. The mass-weighted averages of the five sections are shown for each type of changes. Changes exceeding one ensemble standard deviation are deemed statistically significant and is presented in bold.

$0.08 \pm 0.02 \text{ mol m}^{-2} \text{ yr}^{-1}$. This is likely due to increased ventilation of SAMW, which enhances the sequestration of young C_{ANT} -rich water, dominating over the increased upwelling in the Southern Ocean which transports old, low- C_{ANT} water into CDW. We see that a significant proportion of changes in C_{ANT} attributable to changes in \mathcal{G} (14%), showing the importance of accounting for circulation changes when estimating evolution of C_{ANT} .

CHAPTER 5

Discussions and Conclusions

The boundary propagator, \mathcal{G} , is the integral representation of the transport operator for transport from the surface ‘boundary’ into the ocean interior. As such, \mathcal{G} contains complete information on surface-to-interior transport. \mathcal{G} is a distribution that partitions every water parcel in the interior ocean according to location of last ventilation and the transit time from that location. Once the boundary propagator at an interior point is known, one can easily convolve it with the surface history of any tracer of interest to yield the tracer’s concentration at that point. Using a maximum entropy (ME) approach, we deconvolve tracer measurements for the boundary propagator \mathcal{G} in the Southern Ocean, and we estimate the change of \mathcal{G} from the early 1990s to the mid-2000s. The ME method gives the most objective estimate of \mathcal{G} based on tracers alone that is maximally non-committal to missing information. We emphasize that in estimating \mathcal{G} , the method does not assume a steady circulation. Also, our method of quantifying C_{ANT} does not rely on any empirical relationships between C_{ANT} and other tracers.

Our results on the water-mass source regions and ideal mean age in the early 1990s are broadly consistent with existing studies. *Gebbie and Huybers* [2010] used what they call *the total matrix intercomparison* (TMI) to invert WOCE climatology compiled from measurements taken mostly in the 1990s [*Gouretski and Koltermann*, 2004] to solve for transport pathways into the global ocean interior. The TMI method and our method give similar estimates

for the water-mass fractions last ventilated between SB and STF: 60–70% in the Southern Ocean between 250–1500 m depth. The TMI method, however, gave an estimate of ∼40% for the water-mass fraction in the Southern Ocean last ventilated south of SB, which is considerably smaller than our estimate of ∼60%. Our results for the water-mass fractions closely match the data-assimilated model estimates of *DeVries and Primeau* [2011] (notwithstanding slightly different definitions of surface regions) and the estimates of the global mean transit time are within ∼100 yr of each other. It is possible that this close agreement is the result of our prior containing coarse-grained transport information from this model. Other studies quantify mixing based on eddy kinetic energy [EKE; e.g., *Wilkin and Morrow*, 1994; *Meredith and Hogg*, 2006; *Zika et al.*, 2013]. This is related, but distinct from the measure of Δ/Γ , which increases only when waters with a wide range of transit times are mixed together. However, our results do show increased Δ/Γ in the vicinity of SAF and PF and within STMW in the vicinity of subtropical gyres, coinciding with regions of high EKE (e.g., the model and observation study of *Delworth et al.* [2012]). To the best of our knowledge, this thesis is the first study to examine the spatial variation of Δ/Γ in the ocean interior. This is an improvement over the study of *Waugh et al.* [2004] that gave a single number estimate of $\Delta/\Gamma \sim 1$ for the subpolar North Atlantic Ocean, based on tritium and CFC measurements.

Our results on the decadal changes in ventilation extend the knowledge from current observational studies and are broadly consistent with poleward-strengthening mid-latitude westerly winds. The general increase in transit time from the surface into CDW, as well as the increased NA-ventilated fraction found in CDW, indicate a stronger upwelling/overturning that may be wind-induced. The shorter transit time into SAMW and the larger SAF-STF fractions found in SAMW indicate an enhanced formation of SAMW due to stronger northward Ekman drift. The changes in ideal mean age that we infer

are in agreement with the findings of *Tanhua et al.* [2013] of younger water-mass age within Section P18 between 33–37°S. Compared to the changes in mean age described by *Waugh* [2014], our $\delta\Gamma/\bar{\Gamma}$ has a considerably more complex structure. This may be due to the extra tracer constraints (CFC-11 in addition to CFC-12) and that we do not assume an inverse-Gaussian TTD. We do however see a clear change in the fraction of water that is older than 30 years, which qualitatively agrees with *Waugh* [2014].

Our result in decadal storage changes in C_{ANT} in the Southern Ocean are similar to some existing studies and but differ from others. The total decadal C_{ANT} change in Section P16 presented in Figure 4.12a agrees well with *Wanninkhof et al.* [2010]’s estimate for the period 1999–2005 (Figure 5 in their work), both in terms of distribution and amplitude of the change. Compared to *Sabine et al.* [2008]’s estimate for Section P16 for the period 1991–2005 (Figure 4 in their work) our result for P16 in Figure 4.12a is similar in spatial pattern but our change has about twice the amplitude. Our result of C_{ANT} column storage increasing by $0.49 \pm 0.02 \text{ mol m}^{-2}\text{yr}^{-1}$ due to increased atmospheric CO₂ loadings is somewhat lower than the corresponding $0.6\text{--}0.8 \text{ mol m}^{-2}\text{yr}^{-1}$ increase estimated by *Khatiwala et al.* [2013]. There are other studies that quantified the C_{ANT} change in terms of the inventory of C_{ANT} integrated across partial or whole basins. We chose not to compare with these studies by extrapolating our along-section estimates to cover the entire basin as doing so would involve additional assumptions and uncontrolled approximations. We note that our estimate of C_{ANT} in the Southern Ocean accounts for C_{ANT} entering from all surface regions of the global ocean. However, our result only relates to C_{ANT} that is stored within the Southern Ocean and does not account for C_{ANT} that entered through the Southern Ocean and is subsequently transported and stored elsewhere in the global ocean.

In a broader picture, the ocean acts as a sink for all carbon, not just C_{ANT} . The total DIC in the ocean is estimated to be about 200 times the total C_{ANT}

inventory [Falkowski *et al.*, 2000; Sabine *et al.*, 2004]. However, because we do not analyze any carbon measurements here, we focus only on estimating the anthropogenic carbon contribution and its decadal changes. While the C_{ANT} storage rate of the ocean is estimated to have increased, the ocean's ability to take up carbon is reported to be weakening in recent decades by both forward [e.g., Lovenduski *et al.*, 2008] and inverse model studies [e.g., Le Quéré *et al.*, 2007]. These studies attribute these changes to the poleward shifting and strengthening mid-latitude westerly winds, which draw up carbon-rich deep waters to release CO₂ into the atmosphere.

It is useful to keep in mind the following limitations of the ME deconvolutions of \mathcal{G} : Our Maximum Entropy approach, like many other observation-based inversion methods [e.g., Tomczak and Large, 1989; Matsumoto, 2007] utilizes tracer constraints but does not explicitly account for dynamical constraints or geometric constraints such as the pathway distance between surface regions and interior points. However, pathway and dynamical information can enter the deconvolution in the form of a prior. Here, we utilized a prior derived from the data-assimilated, *steady* ocean model of Primeau *et al.* [2013]. Deconvolution with our ensemble of perturbed priors (see Section A.4) shows that our key results are driven by the tracer constraints and are not built into the priors. In particular, the priors built from a steady circulation contains no information on decadal changes. Consistency across the ensembles points to the robustness of our results.

The inferences made using our Maximum Entropy approach are only as good as the quality of the observational data. Many tracers can now be accurately measured. However, several approximations have to be made to construct the tracer surface history going back to pre-industrial times. For temperature, salinity, and PO₄^{*}, we have insufficient knowledge of their long-term trend, necessitating a cyclostationary approximation for their surface boundary conditions. We also lack seasonal CFC surface data, necessitating

the use of annual averages. This misses the annual cycle of the CFC concentrations due to the tendency of water to enter the permanent thermocline during late winter [Stommel, 1979; Williams *et al.*, 1995]. The joint use of several tracers (cyclostationary Θ , S_A , PO_4^* and transient CFC's and radiocarbon) allows us to constrain the seasonal, interannual, and longer-time variations in surface-to-interior transit time.

The hydrographic data we use are essentially snapshots in time that encapsulate transport information on all timescales. Therefore, the inferred transport changes most likely contain seasonal and interannual signals as well as decadal signals. We are not able eliminate the seasonal cycle by obtaining a hydrographic dataset for which the original and repeat hydroographies were measured during the same month of the year. Future studies may improve on this by (a) inferring seasonality in transport by deconvolving the WOA09 data set, which contains climatological monthly data for steady tracers, or by (b) using a forward ocean model to estimate both the seasonal and interannual changes.

We applied our analysis of \mathcal{G} and its decadal changes to estimate decadal changes in oceanic C_{ANT} and to determine how much of these changes is due to changes in ventilation and how much is due to changes in atmospheric CO_2 concentration. For simplicity, we assumed a time-invariant surface CO_2 disequilibrium with the atmosphere, as have many other investigators [e.g., Waugh *et al.*, 2006]. We acknowledge this is only an approximation that can lead to biases. Khatiwala *et al.* [2009] addressed this problem by simultaneously solving for the boundary propagator and the air-sea C_{ANT} flux. However, correcting for the relatively small effects of changing disequilibrium is beyond the scope of this thesis.

In summary, the key findings of this thesis research are:

- *Base state of Southern Ocean ventilation in the early 1990s*

We estimated three surface-to-interior transport metrics: The global water-mass fraction older than 30 years, $f(\mathbf{r}, t; 30 \text{ yr})$; the global mean transit time, $\Gamma(\mathbf{r}, t)$; and the ratio of Δ/Γ , which quantifies the broadness of the regional TTD on the scale of Γ . The value of Δ/Γ thus provides a measure of the mixing of fluid elements with a multitude of paths from Ω to the point of observation. Water younger than 30 yr comprises most of STMW as well as the part of SAMW closest to its subduction zone and penetrates as deep as $\sim 1500\text{m}$. Water older than 30 years comprises almost all of CDW, consistent with CDW being an upwelling water-mass. The mean transit time of LCDW is estimated to be 300–400 yr. For SAMW, $\Gamma(\mathbf{r}, t_1)$ grows from near zero at the outcrop, to more than 50 years by $\sim 30^\circ\text{S}$ after the water mass subducts, finally reaching up to 100–300 years in the tropics depending on the basin. NADW in the Atlantic basin is relatively young (up to 200 years), while deep waters in the Pacific and Indian Ocean are up to 1000 years old. A ratio of Δ/Γ between 0.5–2 is ubiquitous in the Southern Ocean between 500–1500m depth. Within STMW and the upper 750m of CDW, Δ/Γ is larger than 2, indicating that STMW and CDW are admixtures of waters with a wide spectrum of transit times since last ventilation.

Within key water masses, the fractions last ventilated in different surface regions, as well as the fractions' regional mean transit time, are estimated. Up to 70% of CDW was last ventilated in the vicinity of the Antarctic shelf, mixed with up to 20% (50% in the Atlantic sector) last ventilated in the North Atlantic. Up to 70% of AAIW was last ventilated between SB and SAF. SAMW is mostly comprised of water last ventilated between SAF and STF, confirming the picture provided by *Hanawa and Talley* [2001]. 50–100% of STMW is dominated by the OTHER fraction (water ventilated outside the Southern Ocean and North Atlantic). The Atlantic sector STMW also contains a moderate NA fraction (up to 20%). The water-mass fractions last ventilated

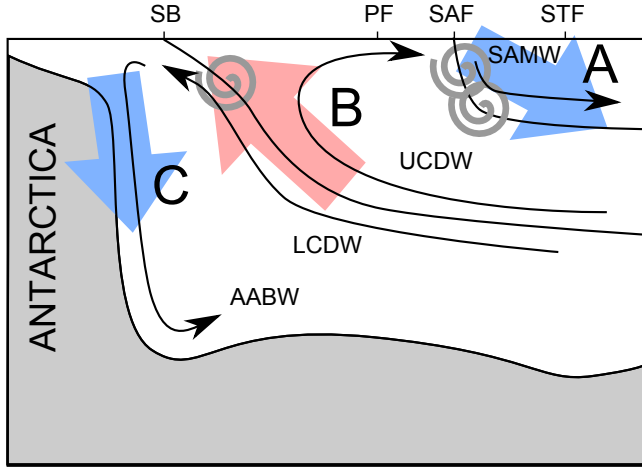


Figure 5.1: A schematic summarizing the key decadal changes found in this study. A: Higher fraction of younger water last ventilated between SAF and STF found in SAMW. B: Higher fraction of older water last ventilated in the North Atlantic found in CDW. C: Younger AABW. The red (blue) colour of the big arrows indicates an increase (decrease) in the water mass' transit time.

in the Southern Ocean regions (i.e., south of SB, SB-SAF and SAF-STF) have similar regional mean-age patterns $\Gamma_{\Omega_i}(\mathbf{r})$ and have a regional mean age of less than 200yr within SAMW. Water last ventilated south of SB takes an average of 200–400yr to enter CDW and takes on average 800–1000yr to enter deep tropics. Water last ventilated in the North Atlantic takes on average 100–200yr to cross the equator, 400–600yr to enter LCDW, 1000–1200yr to enter the deep South Pacific, and 1200–1400yr to enter the deep tropical Indian Ocean.

- *Decadal changes in Southern Ocean ventilation between early 1990s and mid-2000s*

We find a distinct dipolar pattern in $\delta f(\mathbf{r}; 30\text{yr})$: an increase of $\sim 20\%$ per decade within CDW and a decrease of $\sim 10\%$ decade within SAMW and STMW north of 40°S , the approximate latitude where the isopycnals cease sloping down towards north. In line with the pattern of $\delta f(\mathbf{r}; 30\text{yr})$, there is a $\sim 80\%$ per-decade increase in Γ of water south of 40°S and a corresponding $\sim 80\%$ decree in Γ of water north of 40°S . Additionally, the global mean transit time in Sections P16 and P18 at $\sim 60^\circ\text{S}$ has decreased by 40–80% per decade. Widespread Γ increase by $\sim 40\%$ per decade occurred in section A16. Δ/Γ has

undergone significant decadal changes with a \sim 20% decrease within AAIW and a \sim 40% increase within SAMW and STMW.

We identified the following key decadal changes in Southern Ocean water-mass fractions: The fraction of SAF-STF-ventilated water within SAMW and STMW has increased by 7–15% per decade, replacing water ventilated outside of the Southern Ocean and North Atlantic (i.e., the OTHER fraction). Similarly, North Atlantic ventilated water within CDW has increased by \sim 3% per decade, replacing water last ventilated in the south-of-SB and the SB-SAF regions. The ideal mean age of the NA and OTHER fractions within CDW has decreased by \sim 30% per decade. By contrast, the Southern Ocean ventilated fractions within the Atlantic sector of CDW become \sim 60% older per decade. The ideal mean age of lighter SAMW ($\sigma_0 \leq 27 \text{ kg m}^{-3}$) north of 40°S decreases by \sim 60–90% per decade regardless of where the water was last ventilated. This quantifies faster surface-to-interior transport of SAMW north of 40°S and increased upwelling of older waters south of 40°S (see also the schematic of Figure 5.1).

By partitioning the changes of global mean transit time (global mean ‘age’) into contributions from changes in water-mass fractions and from changes in regional mean ages, we infer that the increase in the global mean age of CDW is due to increased regional mean age of Southern Ocean-ventilated water and an increased fraction of old NA-ventilated water. Similarly, the decrease in the global mean age of SAMW and STMW is due to the decreased regional mean age of Southern Ocean-ventilated water and a reduced fraction of NA-ventilated water. For the southernmost Pacific, the decrease in global mean age is due to the decreased regional mean age of SO-ventilated water, as well as due to a decreased fraction and decreased regional mean age of OTHER water. The widespread increase of the global mean age into South Atlantic SAMW is also due to the increased regional mean age of OTHER water.

Our results are largely consistent with the expected change in transport given poleward-intensified mid-latitudes westerlies. Within CDW, an increased NA water-mass fraction, an increased fraction older than 30 years (regardless of origin), and an increased global mean age are all consistent with increased upwelling of CDW. Also, within SAMW and STMW, an increased Southern Ocean water-mass fraction, an increased fraction younger than 30 years, and a decreased global mean age, are all consistent with greater northward Ekman drift into SAMW and higher AAIW formation rate. The increased Δ/Γ of the age distribution of SAMW may also indicate an enhanced eddy field and increased mixing.

- *Transport-induced decadal changes in anthropogenic carbon in Southern Ocean*

We propagate the increasing atmospheric CO₂ history since the industrial revolution into the the Southern Ocean interior to obtain an estimate the decadal changes in the oceanic C_{ANT} concentration. By using independently deconvolved \mathcal{G} s at two observation times, we are able to infer the part of the decadal changes in C_{ANT} due to changes in ventilation (and not atmospheric CO₂ increases). The total increase from the early 1990s to mid-2000s is estimated at $\sim 13 \mu\text{mol kg}^{-1}\text{decade}^{-1}$. Changes in the surface-to-interior transport act to decrease the C_{ANT} within CDW by up to $5 \mu\text{mol kg}^{-1}\text{decade}^{-1}$ and increase the C_{ANT} concentration within SAMW and STMW by up to $\sim 5 \mu\text{mol kg}^{-1}\text{decade}^{-1}$. In terms of the column C_{ANT} storage change per unit area, an average storage increase of $0.56 \pm 0.02 \text{ mol m}^{-2} \text{ yr}^{-1}$ is found in the Southern Ocean between 60–20°S. Changes in \mathcal{G} are not found to significantly affect the C_{ANT} storage south of 40°S, but act to increase the C_{ANT} storage by $0.116 \pm 0.006 \text{ mol m}^{-2} \text{ yr}^{-1}$ north of 40°S. Summing over the latitudes between 60–20°S, changes in ventilation act to increase the C_{ANT} storage by $0.08 \pm 0.02 \text{ mol m}^{-2} \text{ yr}^{-1}$, which

is 14% of the total C_{ANT} uptake in the Southern Ocean. In short, the recent decadal changes in the Southern Ocean ventilation acts to enhance C_{ANT} uptake in the Southern Ocean.

APPENDIX A

Details of MEM set up

A.1 Discretization details

Spatially, we partition the ocean surface \mathbf{r}_s into $3^\circ \times 3^\circ$ grid boxes indexed by s . For transit time, since most of the seasonal data are in monthly averages, we break down the years into 12 months. We use n to denote the number of whole years in the transit time, and m to denote the calendar months in that year, with 1 being December and 12 being January (notice the reversed ordering). Our month and year discretization are $m = 1, \dots, 12$ and $n \in \{0, 1, 2, 3, 6, 9, \dots, 75, 80, 90, 120, 160, 200, 250, 300, 400, 500, \dots, 1000, 1200, 1500, 2000, 2500, \dots, 4000, 5000, 7000, 9000, 11000, 15000, 20000\}$.

A.2 Standardizing C^S and C^I

Our ME method requires the Lagrange multipliers λ_j in (2.9) to be found numerically by solving (2.8) simultaneously. For numerical stability we center and scale the C_j^S and C_j^I , and here we show that the resultant ME solution is identical to that obtained without standardizing the tracer constraints, notwithstanding numerical errors.

Suppose we are solving for \mathcal{P} for the set of tracer constraints

$$\sum_{m,n,s} w_n \mathcal{P} C_j^S = C_j^I \quad \text{for } j = 1, \dots, J, \tag{A.1}$$

If we write $C_j^S(m, n, s) = c_j + \sigma_j \hat{C}_j^S(m, n, s)$, where c_j, σ_j are respectively the mean and standard deviations of C_j^S , then the ME expression becomes

$$\begin{aligned}
\mathcal{P} &= \frac{\mu \exp\left(-\sum_{j=1}^J \lambda_j C_j^S\right)}{\sum_{m,n,s} w_n \mu \exp\left(-\sum_{j=1}^J \lambda_j C_j^S\right)} \\
&= \frac{\mu \exp\left(-\sum_{j=1}^J \lambda_j (c_j + \sigma_j \hat{C}_j^S)\right)}{\sum_{m,n,s} w_n \mu \exp\left(-\sum_{j=1}^J \lambda_j (c_j + \sigma_j \hat{C}_j^S)\right)} \\
&= \frac{\exp\left(-\sum_{j=1}^J \lambda_j c_j\right) \mu \exp\left(-\sum_{j=1}^J \lambda_j \sigma_j \hat{C}_j^S\right)}{\exp\left(-\sum_{j=1}^J \lambda_j c_j\right) \sum_{m,n,s} w_n \mu \exp\left(-\sum_{j=1}^J \lambda_j \sigma_j \hat{C}_j^S\right)} \\
&= \frac{\mu \exp\left(-\sum_{j=1}^J \lambda_j \sigma_j \hat{C}_j^S\right)}{\sum_{m,n,s} w_n \mu \exp\left(-\sum_{j=1}^J \lambda_j \sigma_j \hat{C}_j^S\right)}
\end{aligned} \tag{A.2}$$

and a unique set of λ_j can then be obtained numerically, if a ME solution exists.

Suppose now we are instead given the following set of tracer constraints to solve for the Lagrange multipliers:

$$\sum_{m,n,s} w_n \mathcal{P} \hat{C}_j^S = \hat{C}_j^I \quad \text{for } j = 1, \dots, J, \tag{A.3}$$

where $\hat{C}_j^I \equiv (C_j^I - c_j) / \sigma_j$ are also standardized using the means and standard deviations from the surface history. The ME expression would then be

$$\hat{\mathcal{P}} = \frac{\mu \exp\left(-\sum_{j=1}^J \hat{\lambda}_j \hat{C}_j^S\right)}{\sum_{m,n,s} w_n \mu \exp\left(-\sum_{j=1}^J \hat{\lambda}_j \hat{C}_j^S\right)} \tag{A.4}$$

(the hats above λ_j and \mathcal{P} have been added to emphasize that these are new quantities from the problem with \hat{C}_j^S and \hat{C}_j^I as the tracer constraints). Note that (A.4) has the same form as (A.2) except a constant σ_j beside every Lagrange multiplier λ_j . By the uniqueness of \mathcal{P} [Jaynes, 1963] and the Lagrange

multipliers (Proposition 2.3.2), we deduce that $\hat{\mathcal{P}} \equiv \mathcal{P}$, with $\hat{\lambda}_j = \sigma_j \lambda_j$ for all j . In another word, the ME boundary propagator obtained by solving the standardized tracer constraints is identical to its non-standardized counterpart, with their Lagrange multipliers related by the scale of the constraints. Note that the ME solution (even the Lagrange multipliers) are independent of the mean c_j .

Standardizing the constraints before solving the problem is important. Tests showed that MATLAB fsolve can fail to converge to a solution should the means or standard deviations of the constraints differ by a scale of ~ 100 or more.

A.3 Fsolve set up

We use the MATLAB fsolve routine to solve our systems of nonlinear equations. Now fsolve requires the equation of interest to be in the form of $\mathbf{F}(\lambda) = \mathbf{0}$, where λ is a vector of variables to be solved for. Also, it can take the Jacobian $J_{\mathbf{F}}(\lambda)$ to improve efficiency.

Our set of equations for fsolve is:

$$F_j(\lambda) = \hat{C}_j^I(\lambda) - C_j^I = 0 \quad \text{for all } j = 1, \dots, J,$$

where

$$\hat{C}_j^I(\lambda) \equiv \sum_{m,n,s} w_n \hat{\mathcal{P}}(m, n, s; \lambda) C_j^S(m, n, s)$$

and

$$\mathcal{P}(m, n, s; \lambda) = \frac{Y(m, n, s; \lambda)}{Z(\lambda)}$$

where $Y(m, n, s; \lambda) = \mu(m, n, s) \exp\left(-\sum_j \lambda_j C_j^S(m, n, s)\right)$ and $Z(\lambda) = \sum_{m,n,s} w_n Y$.

$$\text{Now } \frac{\partial F_j}{\partial \lambda_k} = \frac{\partial \hat{C}_j^I}{\partial \lambda_k} = \sum_{m,n,s} w_n \frac{\partial \hat{\mathcal{P}}}{\partial \lambda_k} C_j^S(m, n, s)$$

Now

$$\frac{\partial Y}{\partial \lambda_k} = -C_k^S Y$$

(w_n is the weight in the numerical quadrature over transit time) and

$$\begin{aligned}\frac{\partial Z}{\partial \lambda_k} &= \sum_{m,n,s} w_n \frac{\partial Y}{\partial \lambda_k} \\ &= - \sum_{m,n,s} w_n C_k^S(m, n, s) Y(m, n, s)\end{aligned}$$

Then

$$\begin{aligned}\frac{\partial \mathcal{P}}{\partial \lambda_k} &= \frac{Y}{Z} \left(\frac{\partial Y}{\partial \lambda_k}/Y - \frac{\partial Z}{\partial \lambda_k}/Z \right) \\ &= \mathcal{P} \left(-C_k^S Y/Y - \sum_{m,n,s} w_n C_k^S(m, n, s) Y(m, n, s)/Z \right) \\ &= \mathcal{P} \left(-C_k^S + \sum_{m,n,s} w_n C_k^S(m, n, s) \mathcal{P} \right) \\ &= \mathcal{P}(m, n, s) \left(-C_k^S(m, n, s) + \hat{C}_k^I \right)\end{aligned}$$

So

$$\frac{\partial F_j}{\partial \lambda_k} = \frac{\partial \hat{C}_j^I}{\partial \lambda_k} = \sum_{m,n,s} w_n C_j^S(m, n, s) \mathcal{P}(m, n, s) \left(\hat{C}_k^I - C_k^S(m, n, s) \right)$$

A.4 Perturbation of the prior

As a test of robustness of the results i.e. how much of the results is data-driven and independent of prior information, we deconvolve the tracer constraints using an ensemble of perturbed priors. For the time dependence, we substitute $\tau_{m,n}$ in (3.1) for $\tau_{m,n}/\alpha$ for $\alpha < 1$ and $\alpha > 1$, i.e. 'squeezing' and 'stretching' the inverse Gaussian prior which in effects decreases or increases the mean transit time. For the spatial dependence, we randomly change the source contribution by substituting $f_M(\mathbf{r}; l)$ in (3.1) for $f_M(\mathbf{r}; l)\beta_l/Z$, where β_l are independently drawn from a uniform distribution ranging from $1 - \gamma$ to $1 + \gamma$, γ controls the scale of the perturbation and Z is a normalization constant so that $\sum_{l=1}^{14} f_M(\mathbf{r}, l) = 1$. Such perturbation scheme means that watermass

fractions that are close to 0 or 1 would be modified less, while fraction that are further from 0 or 1 would be modified more. We permute 3 temporal perturbation cases ($\alpha = 0.5, 1, 2$) with 5 spatial perturbation cases (5 sets of randomly generated $\{\beta_l\}_{l=1}^{14}$ using the scale parameter $\gamma = 0.9$) to form the 15-member ensemble.

APPENDIX B

Determination of an optimal ‘nominal year’ for GLODAP transient tracers

Recall from Section 3.1 that our CFCs boundary condition is constructed from the GLODAP CFC annual mean climatology, scaled by $\text{CFC}(y_n)_A/\text{CFC}(y_{\text{GLODAP}})_A$, where $\text{CFC}(y_n)_A$ is the measured global annual mean atmospheric concentration for year y_n . To do this, we need to associate the GLODAP climatology with a single observation year, y_{GLODAP} . *Key et al.* [2004] reported that the GLODAP CFC gridded data sets were aggregated from observations made between 1985–1999, and *Sabine et al.* [2004] designated the approximate median year of the oceanographic measurements, 1994, as the nominal year of the GLODAP CFC dataset y_{GLODAP} . However, within the period that observations were taken, atmospheric CFC concentrations have increased [*Fine, 2011*], which would result in a rising trend in the oceanic CFC measurements. However, *Key et al.* [2004] noted that no attempt was made to adjust for this trend. This implies that (1) the use of a nominal year is a rather uncontrolled approximation, and that (2) the optimal y_{GLODAP} needed to construct our boundary condition may not be 1994.

When we use $y_{\text{GLODAP}} = 1994$, our initial attempt to include both CFC-11 and CFC-12 along with four other tracer constraints failed because no solution for all Lagrange multipliers could be found. (Our early work therefore did not use CFC-11). Further, our deconvolved \mathcal{G} using only CFC-11 plus the other four constraints consistently under-predicted CFC-12 decadal changes $\Delta\delta C$, as

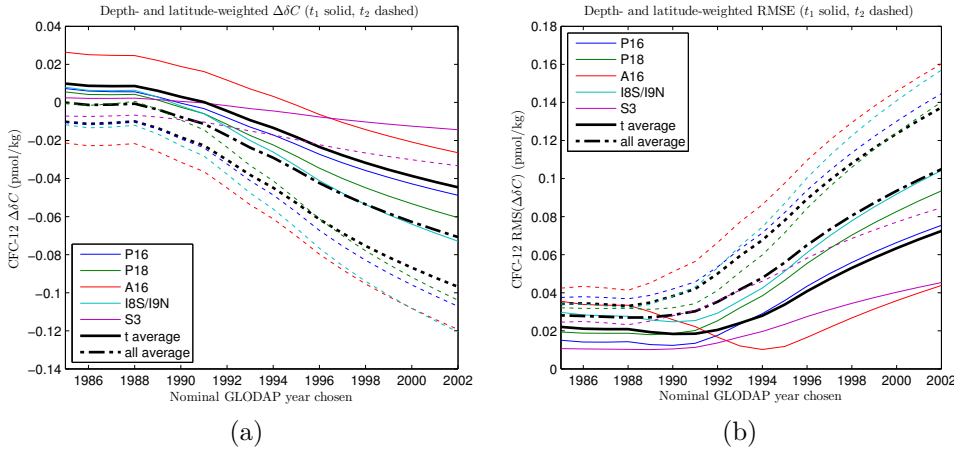


Figure B.1: (a) Errors and (b) root-mean-squared errors in the predicted CFC-12 decadal changes, as a functions of y_{GLODAP} chosen.

can also be seen in the ME study of *Holzer et al.* [2010] who employed a similar suite of hydrographic data to infer \mathcal{G} for Section A20 in the northwestern Atlantic ocean.

We therefore investigated the effects of changing y_{GLODAP} and determined an optimal value for y_{GLODAP} by minimizing $\Delta\delta C$ as a function of y_{GLODAP} as shown in Figure C.2. The errors are minimal for y_{GLODAP} earlier than ~ 1990 for all hydrography sections apart from the t_1 curve for Section A16. When weighting all 10 hydrography sections by volume defined by a one-degree longitude swath around the section, we determined the optimal y_{GLODAP} to be 1988. Figure B.2b shows $\Delta\delta C$ for $y_{GLODAP} = 1988$, which is slightly smaller magnitude than $\Delta\delta C$ for $y_{GLODAP} = 1994$ (Figure B.2a). Most importantly, however, using $y_{GLODAP} = 1988$ allows us to deconvolve for \mathcal{G} using both CFC-11 and CFC-12 in addition to the other four tracers. All results in the text correspond to this six-tracer deconvolution with $y_{GLODAP} = 1988$.

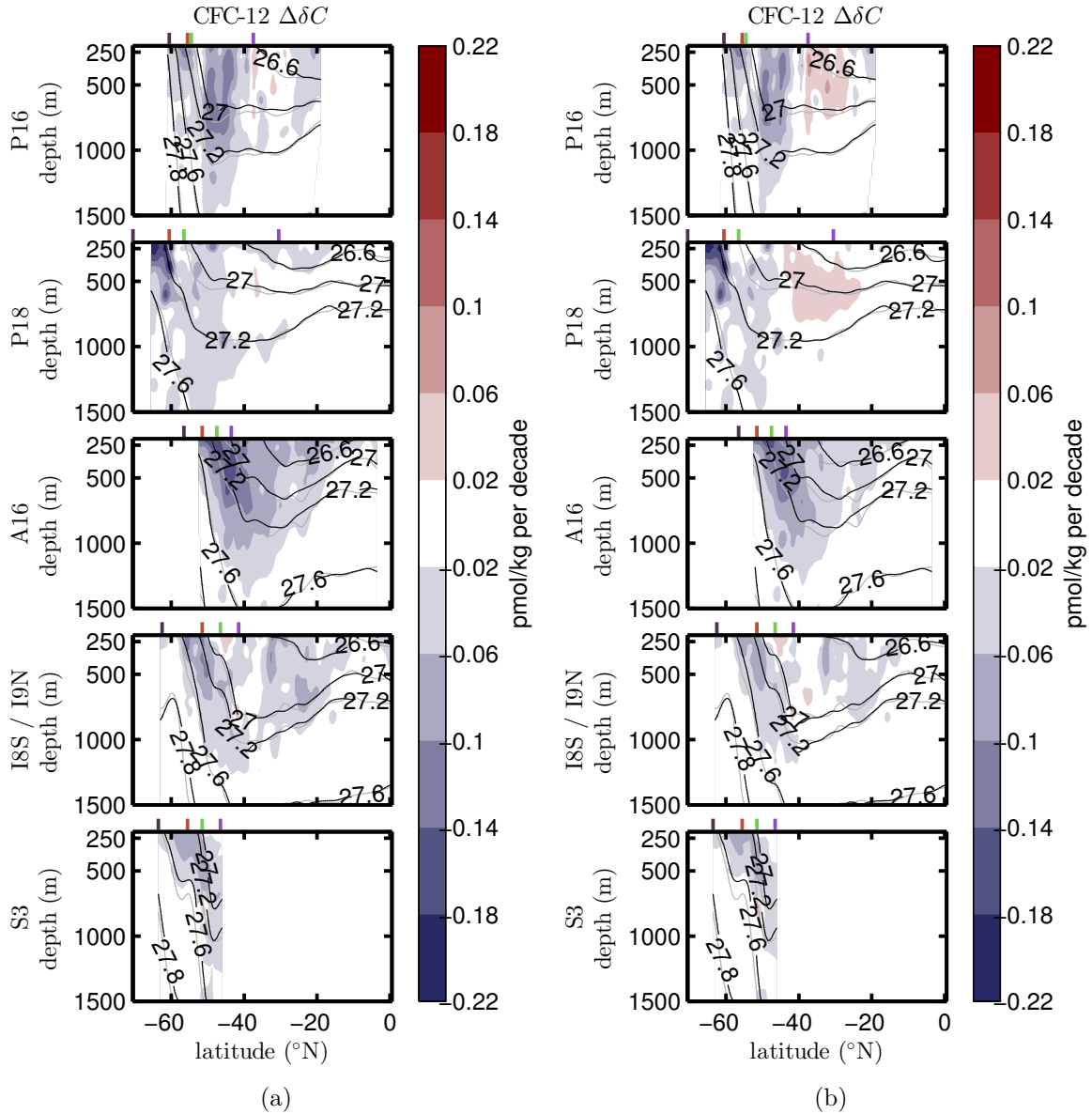


Figure B.2: Errors in the predicted CFC-12 decadal changes using (a) $y_{GLODAP} = 1994$ (b) $y_{GLODAP} = 1988$. See Figure 4.1 for potential density anomaly contours and ticks definitions.

APPENDIX C

Supplementary figures

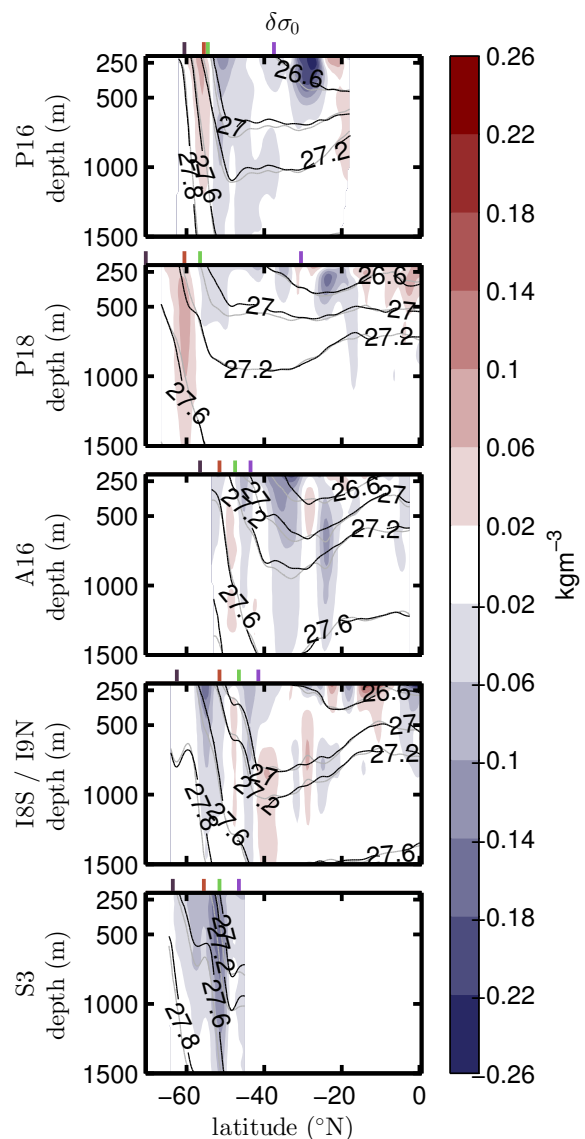


Figure C.1: Changes in density anomaly between times of original and repeat hydrography. Isopycnals of t_1 are shown in black contours while isopycnals of t_2 are shown in grey. See Figure 4.1 for ticks definitions.

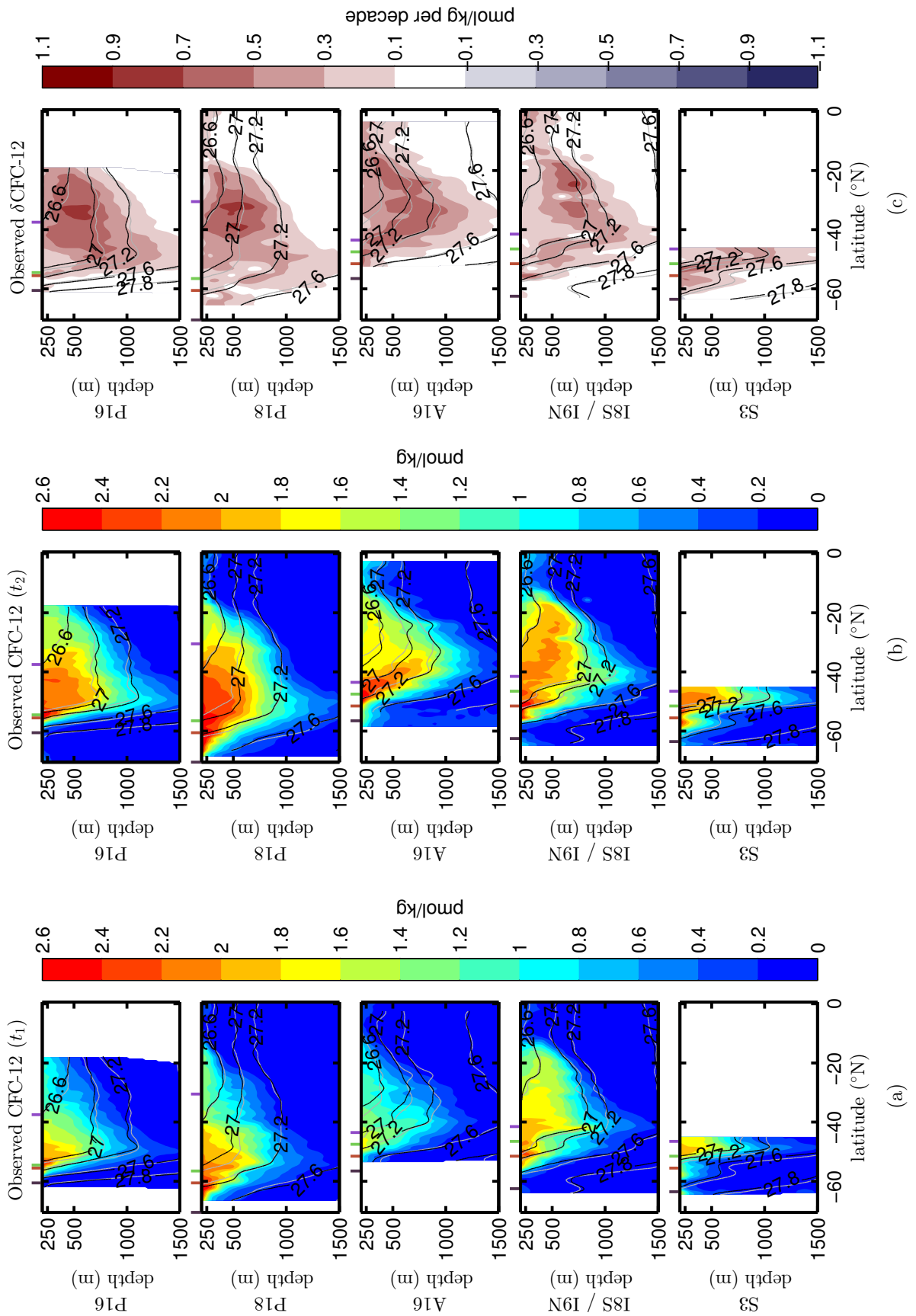


Figure C.2: (a,b) Observed CFC-12 interior concentration at t_1 and t_2 respectively. (b) Observed CFC-12 difference. See Figure 4.1 for potential density anomaly contours and ticks definitions.

Bibliography

- Antonov, J. I., D. Seidov, T. P. Boyer, R. A. Locarnini, A. V. Mishonov, H. E. Garcia, O. K. Baranova, M. M. Zweng, and D. R. Johnson, *World Ocean Atlas 2009, Volume 2: Salinity*, U.S. Government Printing Office, 2010.
- Brewer, P. G., Direct observation of the oceanic co₂ increase, *Geophysical Research Letters*, 5(12), 997–1000, 1978.
- Broecker, W., et al., How much deep water is formed in the southern ocean?, *Journal of Geophysical Research*, 103(15), 833–15, 1998.
- Caldeira, K., and P. B. Duffy, The role of the southern ocean in uptake and storage of anthropogenic carbon dioxide, *Science*, 287(5453), 620–622, 2000.
- Chen, G.-T., and F. J. Millero, Gradual increase of oceanic co₂, 1979.
- Ciais, P., et al., Carbon and other biogeochemical cycles, in *Climate Change 2013: The Physical Science Basis. Contribution of Working Group I to the Fifth Assessment Report of the Intergovernmental Panel on Climate Change*, pp. 465–570, Cambridge University Press, 2014.
- Delworth, T. L., et al., Simulated climate and climate change in the gfdl cm2.5 high-resolution coupled climate model, *Journal of Climate*, 25(8), 2755–2781, 2012.
- DeVries, T., and F. Primeau, Dynamically and observationally constrained estimates of water-mass distributions and ages in the global ocean, *Journal of Physical Oceanography*, 41(12), 2381–2401, 2011.
- England, M. H., J. S. Godfrey, A. C. Hirst, and M. Tomczak, The mechanism for antarctic intermediate water renewal in a world ocean model, *Journal of Physical Oceanography*, 23(7), 1553–1560, 1993.

- Falkowski, P., et al., The global carbon cycle: a test of our knowledge of earth as a system, *science*, 290(5490), 291–296, 2000.
- Fine, R. A., Tracers, time scales, and the thermohaline circulation: The lower limb in the north atlantic ocean, *Reviews of Geophysics*, 33(S2), 1353–1365, 1995.
- Fine, R. A., Observations of cfcs and sf6 as ocean tracers, *Annual review of marine science*, 3, 173–195, 2011.
- Fogt, R. L., J. Perlwitz, A. J. Monaghan, D. H. Bromwich, J. M. Jones, and G. J. Marshall, Historical sam variability. part ii: Twentieth-century variability and trends from reconstructions, observations, and the ipcc ar4 models*, *Journal of Climate*, 22(20), 5346–5365, 2009.
- Friis, K., A. Körtzinger, J. Pätsch, and D. W. Wallace, On the temporal increase of anthropogenic co 2 in the subpolar north atlantic, *Deep Sea Research Part I: Oceanographic Research Papers*, 52(5), 681–698, 2005.
- Garcia, H. E., R. A. Locarnini, T. P. Boyer, J. I. Antonov, O. K. Baranova, M. M. Zweng, and D. R. Johnson, *World Ocean Atlas 2009, Volume 3: Dissolved Oxygen, Apparent Oxygen Utilization, and Oxygen Saturation*, U.S. Government Printing Office, 2010a.
- Garcia, H. E., R. A. Locarnini, T. P. Boyer, J. I. Antonov, M. M. Zweng, O. K. Baranova, and D. R. Johnson, *World Ocean Atlas 2009, Volume 4: Nutrients (phosphate, nitrate, silicate)*, U.S. Government Printing Office, 2010b.
- Gebbie, G., and P. Huybers, Total matrix intercomparison: A method for determining the geometry of water-mass pathways, *J. Phys. Oceanogr.*, 40(8), 1710–1728, doi:10.1175/2010JPO4272.1, 2010.
- Gong, D., and S. Wang, Definition of antarctic oscillation index, *Geophysical Research Letters*, 26(4), 459–462, 1999.
- Gouretski, V., and K. P. Koltermann, Woce global hydrographic climatology, *Berichte des BSH*, 35, 1–52, 2004.

- Gruber, N., J. L. Sarmiento, and T. F. Stocker, An improved method for detecting anthropogenic CO₂ in the oceans, *Global Biogeochemical Cycles*, 10(4), 809–837, 1996.
- Haine, T. W., and T. M. Hall, A generalized transport theory: Water-mass composition and age, *Journal of physical oceanography*, 32(6), 1932–1946, 2002.
- Hall, T. M., and R. A. Plumb, Age as a diagnostic of stratospheric transport, *J. Geophys. Res.*, 99(D1), 1059–1070, 1994.
- Hanawa, K., and L. D. Talley, Mode waters, *International Geophysics Series*, 77, 373–386, 2001.
- Hogg, A. M., M. P. Meredith, D. P. Chambers, E. P. Abrahamson, C. W. Hughes, and A. K. Morrison, Recent trends in the southern ocean eddy field, *Journal of Geophysical Research: Oceans*, 2014.
- Holzer, M., and T. Hall, Transit-time and tracer-age distributions in geophysical flows, *Journal of the atmospheric sciences*, 57(21), 3539–3558, 2000.
- Holzer, M., and F. W. Primeau, The diffusive ocean conveyor, *Geophysical research letters*, 33(14), 2006.
- Holzer, M., and F. W. Primeau, Global teleconnections in the oceanic phosphorus cycle: Patterns, paths, and timescales, *Journal of Geophysical Research: Oceans*, 118(4), 1775–1796, doi:10.1002/jgrc.20072, 2013.
- Holzer, M., F. Primeau, W. Smethie Jr, and S. Khatiwala, Where and how long ago was water in the western north atlantic ventilated? maximum entropy inversions of bottle data from woce line a20, *J. Geophys. Res.*, 115, C07,005, 2010.
- Jaynes, E. T., Information theory and statistical mechanics, *Physical review*, 106(4), 620, 1957.
- Jaynes, E. T., Information theory and statistical mechanics (notes by the lecturer), in *Statistical Physics 3*, vol. 1, p. 181, 1963.

Key, R., et al., A global ocean carbon climatology: Results from global data analysis project (glodap), *Global Biogeochemical Cycles*, 18(4), GB4031, 2004.

Khatiwala, S., F. Primeau, and T. Hall, Reconstruction of the history of anthropogenic co₂ concentrations in the ocean, *Nature*, 462(7271), 346–349, 2009.

Khatiwala, S., F. Primeau, and M. Holzer, Ventilation of the deep ocean constrained with tracer observations and implications for radiocarbon estimates of ideal mean age, *Earth and Planetary Science Letters*, 325-326(0), 116 – 125, doi:10.1016/j.epsl.2012.01.038, 2012.

Khatiwala, S., et al., Global ocean storage of anthropogenic carbon, *Biogeosciences*, 10(4), 2169–2191, 2013.

Le Quéré, C., et al., Saturation of the southern ocean co₂ sink due to recent climate change, *Science*, 316(5832), 1735–1738, doi:10.1126/science.1136188, 2007.

Levine, N. M., S. C. Doney, R. Wanninkhof, K. Lindsay, and I. Y. Fung, Impact of ocean carbon system variability on the detection of temporal increases in anthropogenic co₂, *Journal of Geophysical Research: Oceans (1978–2012)*, 113(C3), 2008.

Locarnini, R. A., A. V. Mishonov, J. I. Antonov, T. P. Boyer, H. E. Garcia, O. K. Baranova, M. M. Zweng, and D. R. Johnson, *World Ocean Atlas 2009, Volume 1: Temperature*, NOAA Atlas NESDIS 68, U.S. Government Printing Office, 2010.

Lovenduski, N. S., N. Gruber, S. C. Doney, and I. D. Lima, Enhanced co₂ outgassing in the southern ocean from a positive phase of the southern annular mode, *Global Biogeochemical Cycles*, 21(2), 2007.

Lovenduski, N. S., N. Gruber, and S. C. Doney, Toward a mechanistic understanding of the decadal trends in the southern ocean carbon sink, *Global Biogeochemical Cycles*, 22(3), 2008.

- Marshall, G. J., Trends in the southern annular mode from observations and reanalyses, *Journal of Climate*, 16(24), 4134–4143, 2003.
- Matsumoto, K., Radiocarbon-based circulation age of the world oceans, *Journal of Geophysical Research: Oceans (1978–2012)*, 112(C9), 2007.
- Matsumoto, K., and N. Gruber, How accurate is the estimation of anthropogenic carbon in the ocean? an evaluation of the δc^* method, *Global Biogeochemical Cycles*, 19(3), 2005.
- McCartney, M., Subantarctic mode water, *A voyage of discovery*, 24, 103–119, 1977.
- McDougall, T., and P. Barker, *Getting started with TEOS-10 and the Gibbs Seawater (GSW) Oceanographic Toolbox*, SCOR/IAPSO WG127, 2001.
- Meredith, M. P., and A. M. Hogg, Circumpolar response of southern ocean eddy activity to a change in the southern annular mode, *Geophysical Research Letters*, 33(16), 2006.
- Oke, P. R., and M. H. England, Oceanic response to changes in the latitude of the southern hemisphere subpolar westerly winds, *Journal of Climate*, 17(5), 1040–1054, 2004.
- Orsi, A. H., T. Whitworth III, and W. D. Nowlin Jr, On the meridional extent and fronts of the antarctic circumpolar current, *Deep Sea Research Part I: Oceanographic Research Papers*, 42(5), 641–673, 1995.
- Press, W. H., *Numerical recipes 3rd edition: The art of scientific computing*, Cambridge university press, 2007.
- Primeau, F., and S. Kibler, How much water forms in the southern ocean? a maximum entropy approach to global water mass analysis., in *AGU Fall Meeting Abstracts*, vol. 1, p. 0817, 2008.
- Primeau, F. W., and M. Holzer, The ocean's memory of the atmosphere: Residence-time and ventilation-rate distributions of water masses, *Journal of physical oceanography*, 36(7), 1439–1456, 2006.

- Primeau, F. W., M. Holzer, and T. DeVries, Southern ocean nutrient trapping and the efficiency of the biological pump, *Journal of Geophysical Research: Oceans*, 118(5), 2547–2564, 2013.
- Rintoul, S. R., C. Hughes, and D. Olbers, The antarctic circumpolar current system, *International Geophysics Series*, 77, 271–302, 2001.
- Russell, J. L., K. W. Dixon, A. Gnanadesikan, R. J. Stouffer, and J. Toggweiler, The southern hemisphere westerlies in a warming world: Propping open the door to the deep ocean, *Journal of Climate*, 19(24), 6382–6390, 2006.
- Sabine, C., and N. Gruber, Response to comment on "the ocean sink for anthropogenic co₂", *Science*, 308(5729), 1743, doi:10.1126/science.1109949, 2005.
- Sabine, C. L., R. A. Feely, F. J. Millero, A. G. Dickson, C. Langdon, S. Mecking, and D. Greeley, Decadal changes in pacific carbon, *Journal of Geophysical Research: Oceans*, 113(C7), n/a–n/a, doi:10.1029/2007JC004577, c07021, 2008.
- Sabine, C. L., et al., The oceanic sink for anthropogenic co₂, *science*, 305(5682), 367–371, 2004.
- Sarmiento, J., N. Gruber, M. Brzezinski, and J. Dunne, High-latitude controls of thermocline nutrients and low latitude biological productivity, *Nature*, 427(6969), 56–60, 2004.
- Sarmiento, J. L., *Ocean biogeochemical dynamics*, Princeton University Press, 2013.
- Sarmiento, J. L., T. M. C. Hughes, R. J. Stouffer, and S. Manabe, Simulated response of the ocean carbon cycle to anthropogenic climate warming, *Nature*, 393, doi:10.1038/30455, 1998.
- Shannon, C. E., A mathematical theory of communication, *ACM SIGMOBILE Mobile Computing and Communications Review*, 5(1), 3–55, 2001.
- Steinfeldt, R., M. Rhein, J. L. Bullister, and T. Tanhua, Inventory changes in anthropogenic carbon from 1997–2003 in the atlantic ocean between 20 s and 65 n, *Global Biogeochemical Cycles*, 23(3), 2009.

- Stommel, H., Determination of water mass properties of water pumped down from the ekman layer to the geostrophic flow below, *Proceedings of the National Academy of Sciences*, 76(7), 3051–3055, 1979.
- Swart, N., and J. Fyfe, Observed and simulated changes in the southern hemisphere surface westerly wind-stress, *Geophysical Research Letters*, 39(16), 2012.
- Talley, L. D., Shallow, intermediate, and deep overturning components of the global heat budget, *Journal of Physical oceanography*, 33(3), 530–560, 2003.
- Talley, L. D., G. L. Pickard, W. J. Emery, and J. H. Swift, *Descriptive physical oceanography: an introduction*, Academic Press, 2011.
- Tanhua, T., D. W. Waugh, and J. L. Bullister, Estimating changes in ocean ventilation from early 1990s cfc-12 and late 2000s sf6 measurements, *Geophysical Research Letters*, 40(5), 927–932, 2013.
- Toggweiler, J., and B. Samuels, Is the magnitude of the deep outflow from the atlantic ocean actually governed by southern hemisphere winds?, in *The Global Carbon Cycle*, pp. 303–331, Springer, 1993.
- Toggweiler, J., and B. Samuels, Effect of drake passage on the global thermohaline circulation, *Deep Sea Research Part I: Oceanographic Research Papers*, 42(4), 477–500, 1995.
- Toggweiler, J. R., and J. Russell, Ocean circulation in a warming climate, *Nature*, 451(7176), 286–288, 2008.
- Tomczak, M., and J. S. Godfrey, *Regional oceanography: an introduction*, Pergamon, 1994.
- Tomczak, M., and D. G. Large, Optimum multiparameter analysis of mixing in the thermocline of the eastern indian ocean, *Journal of Geophysical Research: Oceans (1978–2012)*, 94(C11), 16,141–16,149, 1989.
- Trenberth, K. E., J. G. Olson, and W. G. Large, *A global ocean wind stress climatology based on ECMWF analyses*, Climate and Global Dynamics Division, National Center for Atmospheric Research, 1989.

Trenberth, K. E., W. G. Large, and J. G. Olson, The mean annual cycle in global ocean wind stress, *Journal of Physical Oceanography*, 20(11), 1742–1760, 1990.

Walker, S., R. Weiss, and P. Salameh, Reconstructed histories of the annual mean atmospheric mole fractions for the halocarbons cfc-11 cfc-12, cfc-113, and carbon tetrachloride, *Journal of Geophysical Research*, 105(C6), 14,285–14, 2000.

Wallace, D. W., *Monitoring global ocean carbon inventories*, 5, Ocean Observing System Development Panel, 1995.

Wanninkhof, R., S. C. Doney, J. L. Bullister, N. M. Levine, M. Warner, and N. Gruber, Detecting anthropogenic co₂ changes in the interior atlantic ocean between 1989 and 2005, *Journal of Geophysical Research: Oceans (1978–2012)*, 115(C11), 2010.

Waugh, D., T. Hall, B. McNeil, R. Key, and R. Matear, Anthropogenic co₂ in the oceans estimated using transit time distributions, *Tellus B*, 58(5), 376–389, 2006.

Waugh, D. W., Changes in the ventilation of the southern oceans, *Philosophical Transactions of the Royal Society A: Mathematical, Physical and Engineering Sciences*, 372(2019), 20130,269, 2014.

Waugh, D. W., T. M. Hall, and T. W. Haine, Relationships among tracer ages, *Journal of Geophysical Research*, 108(C5), 3138, 2003.

Waugh, D. W., T. W. Haine, and T. M. Hall, Transport times and anthropogenic carbon in the subpolar north atlantic ocean, *Deep Sea Research Part I: Oceanographic Research Papers*, 51(11), 1475–1491, 2004.

Waugh, D. W., F. Primeau, T. DeVries, and M. Holzer, Recent changes in the ventilation of the southern oceans, *science*, 339(6119), 568–570, 2013.

Wilkin, J. L., and R. A. Morrow, Eddy kinetic energy and momentum flux in the southern ocean: Comparison of a global eddy-resolving model with

altimeter, drifter, and current-meter data, *Journal of Geophysical Research: Oceans (1978–2012)*, 99(C4), 7903–7916, 1994.

Williams, R. G., and M. J. Follows, *Ocean dynamics and the carbon cycle: Principles and mechanisms*, Cambridge University Press, 2011.

Williams, R. G., J. C. Marshall, and M. A. Spall, Does stommel's mixed layer "demon" work?, *Journal of Physical Oceanography*, 25(12), 3089–3102, 1995.

Zika, J. D., et al., Vertical eddy fluxes in the southern ocean, *Journal of Physical Oceanography*, 43(5), 941–955, 2013.